PAPER • OPEN ACCESS

Indexing moiré patterns of metal-supported graphene and related systems: strategies and pitfalls

To cite this article: Patrick Zeller *et al* 2017 *New J. Phys.* **19** 013015

New Journal of Physics
The open access journal at the forefront of physics

Deutsche Physikalische Gesellschaft DPG
IOP Institute of Physics

Published in partnership with: Deutsche Physikalische Gesellschaft and the Institute of Physics

OPEN ACCESS

RECEIVED
16 August 2016

REVISED
28 October 2016

ACCEPTED FOR PUBLICATION
14 December 2016

PUBLISHED
13 January 2017

PAPER

Indexing moiré patterns of metal-supported graphene and related systems: strategies and pitfalls

Patrick Zeller[1], **Xinzhou Ma**[2,3] **and Sebastian Günther**[2,4]

[1] Department Chemie, Ludwig-Maximilians-Universität München, Butenandtstr. 5-13, D-81377 Munich, Germany
[2] Chemie Department, Technische Universität München, Lichtenbergstr. 4, D-85748 Garching, Germany
[3] Current address: State Key Laboratory of Optoelectronic Materials and Technologies, School of Material Science and Engineering, Sun Yat-Sen University, Guangzhou 510275, People's Republic of China
[4] Author to whom any correspondence should be addressed.

E-mail: sebastian.guenther@tum.de

Keywords: moiré, graphene, 2-dimensional hexagonal systems, low-energy electron diffraction, x-ray diffraction, scanning tunneling microscopy

Supplementary material for this article is available online

Abstract

We report on strategies for characterizing hexagonal coincidence phases by analyzing the involved spatial moiré beating frequencies of the pattern. We derive general properties of the moiré regarding its symmetry and construct the spatial beating frequency $\vec{K}_{\text{moiré}}$ as the difference between two reciprocal lattice vectors $\vec{k}_i$ of the two coinciding lattices. Considering reciprocal lattice vectors $\vec{k}_i$, with lengths of up to n times the respective (1, 0) beams of the two lattices, readily increases the number of beating frequencies of the nth-order moiré pattern. We predict how many beating frequencies occur in nth-order moirés and show that for one hexagonal lattice rotating above another the involved beating frequencies follow circular trajectories in reciprocal-space. The radius and lateral displacement of such circles are defined by the order n and the ratio x of the two lattice constants. The question of whether the moiré pattern is commensurate or not is addressed by using our derived concept of commensurability plots. When searching potential commensurate phases we introduce a method, which we call cell augmentation, and which avoids the need to consider high-order beating frequencies as discussed using the reported $(6\sqrt{3} \times 6\sqrt{3})R_{30°}$ moiré of graphene on SiC(0001). We also show how to apply our model for the characterization of hexagonal moiré phases, found for transition metal-supported graphene and related systems. We explicitly treat surface x-ray diffraction-, scanning tunneling microscopy- and low-energy electron diffraction data to extract the unit cell of commensurate phases or to find evidence for incommensurability. For each data type, analysis strategies are outlined and avoidable pitfalls are discussed. We also point out the close relation of spatial beating frequencies in a moiré and multiple scattering in electron diffraction data and show how this fact can be explicitly used to extract high-precision data.

1. Introduction

Moiré patterns are generally observed if two lattices are stacked on top of each other, while having either a different lattice constant or a different rotational orientation or both at the same time. The problem has been known in epitaxy and surface science for a long time [1–4], but the topic regained interest after transition metal (TM) catalyzed chemical vapor deposition was identified as a promising growth protocol for graphene (g) [5–8]. The interplay of the real-space geometry of moirés, the corresponding geometry in reciprocal-space and the result on the electronic structure of the corresponding phases led to thorough studies focusing on the description of moirés [9–18]. Due to the hexagonal symmetry of the g-lattice, in particular graphene growth on hexagonally packed TM surfaces and the resulting moiré formation, are of interest [5, 7, 8, 19]. Thus,

throughout this study, we abbreviate the support lattice as TM and the top lattice as g. For the description of similar systems, such as hexagonally packed adsorbates [3, 4, 14] or other hexagonally arranged two-dimensional materials on hexagonally packed support surfaces [20, 21], the nomenclature has been changed accordingly.

Moiré formation may be analyzed by describing the lattices in real-space notation. The question of whether the moiré pattern is commensurate can then be discussed along the following lines. The hexagonal symmetry of the TM- and g-lattices induces a moiré pattern with hexagonal symmetry. If the pattern is commensurate, a hexagonal moiré unit cell exists and is sufficient to characterize the pattern by providing the coordinates of one moiré unit cell vector $\vec{v}_{\text{moiré}}$. Because in the case of commensurability the unit cell vector $\vec{v}_{\text{moiré}}$ must be a vector of both lattices (the TM- and the g-lattices), we can define $\vec{v}_{\text{moiré}}$ as $\vec{v}_{\text{moiré}} = m \times \vec{a}_1 + n \times \vec{a}_2$ and at the same time as $\vec{v}_{\text{moiré}} = r \times \vec{g}_1 + s \times \vec{g}_2$, with $\vec{a}_i$ and $\vec{g}_i$ being unit cell vectors of each hexagonal lattice. This leads to the coordinates $(m, n)_{\text{TM}}$ and $(r, s)_{\text{g}}$, respectively. Choosing a unit cell with 120° angle between the unit cell vectors $\vec{a}_1$ and $\vec{a}_2$ ($\vec{g}_1$ and $\vec{g}_2$), we can calculate the length of the moiré unit cell vector as follows:

$$L_{\text{moiré}} = a_{\text{TM}} \sqrt{m^2 + n^2 - mn} = a_g \sqrt{r^2 + s^2 - rs}\,. \tag{1}$$

Here, a_{TM} and a_{g} represent the length of the respective unit cell vectors (i.e. the lattice constant). The orientation of the unit cell vector with respect to the TM-lattice is given by the angle $\Phi_{\text{moiré,TM}}$ as:

$$\cos(\Phi_{\text{moiré ,TM}}) = \frac{m - \frac{n}{2}}{\sqrt{m^2 + n^2 - mn}}. \tag{2}$$

The orientation of the unit cell with respect to the g-lattice is characterized by the angle $\Phi_{\text{moiré,g}}$ accordingly. It is readily obtained when exchanging (m, n) with (r, s) in equation (2). While it is easy to calculate equations (1) and (2) once the coordinates $(m, n)_{\text{TM}}$ with $(r, s)_{\text{g}}$ are given, it is not a trivial task to find integer numbers (m, n) and (r, s) that fulfill the diophantine equation (1), i.e. there is no easy way of predicting which commensurate moiré cells of coinciding hexagonal lattices are possible.

In a recent publication, we analyzed the moiré formation of two coinciding hexagonal lattices in a more general way, which allowed us to geometrically derive the wanted integer tuples $(m, n)_{\text{TM}}$ and $(r, s)_{\text{g}}$ [11]. For this purpose, we considered lattice functions $f_{\text{TM}}(x, y)$ and $f_{\text{g}}(x, y)$ that consisted of a superposition of sine-wave functions with a defined spatial frequency spectrum. By relating moirés to a stroboscopic experiment, it was shown that the product of the two lattice functions $f_{\text{TM}}(x, y) \times f_{\text{g}}(x, y)$ leads to a pattern with the properties of a moiré. Considering the arbitrary alignment of the two lattices by introducing the rotation R_φ of the f_{g}-lattice by an angle φ with respect to the f_{TM}-lattice, we analyzed the properties of moiré patterns by discussing the function $f_{\text{TM}} \times R_\varphi f_{\text{g}}$. Making use of the so-called convolution theorem in Fourier analysis, we predicted all spatial beating frequencies $\vec{k}_i$ in reciprocal-space, which account for the appearance of the moiré pattern. If the two lattice functions contain reciprocal frequencies $\vec{k}_i$, with a vector length of up to n times the respective (1, 0) beams, a so-called nth-order moiré pattern appears. Spatial beating frequencies in an nth-order moiré pattern appear as the difference vector $\vec{K}_{\text{moiré}} = \vec{k}_{\text{g}} - \vec{k}_{\text{TM}}$, where $\vec{k}_{\text{g}}$ and $\vec{k}_{\text{TM}}$ are the corresponding spatial frequencies of the g- and the TM-lattices. An orientation of the two lattices may be found where two of the spatial frequencies $\vec{k}_{\text{g}}$ and $\vec{k}_{\text{TM}}$ of a given order n (i.e. of a given length) come closest in reciprocal-space leading to the shortest vector $\vec{K}_{\text{moiré}}$. This shortest beating frequency is called the nth-order moiré beating frequency throughout this paper. We should note that for the specific case of first-order lattice frequencies, the spatial beating frequency relating to the longest wavelength was called a moiron by Hermann [9]. Following our general description [11], Hermann also generalized the moiron concept towards higher-order frequencies [22]. Recently, Artaud *et al* extended the description of moiré patterns formed by coinciding hexagonal lattices when allowing for uniaxial strain [12]. The authors used our nomenclature but also introduced a generalized Woods notation of commensurate phases.

In the case where the two lattices develop a commensurate pattern, the moiré has translational symmetry. The smallest possible unit cell of the real-space pattern is then called the moiré unit cell. Knowing all spatial frequencies of an nth-order moiré, we can predict when commensurability sets in and visualize these cases in so-called commensurability plots [11]. We also distinguish the case when spatial beating frequencies approach, but do not exactly reach, the k-space position of a commensurate cell. In such a case a so-called motif of the moiré evolves [23], which may strongly influence the pattern appearance without having the translational symmetry of a lattice.

In the first part of this paper, we discuss the general properties of hexagonal nth-order moiré patterns. Rather than formally solving equation (1), which has to be done by numerical methods, we discuss moiré patterns, their symmetry and potential commensurability in a more general way by addressing their beating frequencies in reciprocal-space. We introduce a so-called cell augmentation technique, which asks for commensurability with respect to an enlarged unit cell in real-space. This techniques is strongly related to the findings of Artaud *et al*

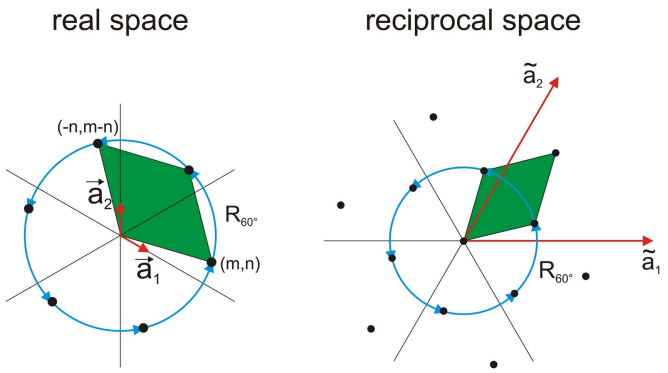

Figure 1. Definition of the coordinate system of the hexagonal lattices and the unit cell of a commensurate superstructure. The lattice unit cell vectors are indicated as $\vec{a}_1$, $\vec{a}_2$ and $\tilde{a}_1$, $\tilde{a}_2$, respectively. The positive rotational direction $(+\varphi)$ is defined as a counterclockwise rotation.

who treated the case of multiple beatings in unit cells [12]. Using the example of the so-called $(6\sqrt{3} \times 6\sqrt{3})R_{30°}$ moiré found for graphene on SiC(0001) [24], we show how cell augmentation avoids the use of high-order beating frequencies when searching for commensurate moiré phases.

In the second part of this paper we apply our method to the moiré analysis of experimental data. For measurements performed by us we provide experimental details in appendix A. In cases where we relate to the interpretation of data acquired by other groups, we direct the reader to the original literature. Within this section, we show how to correctly analyze and index moiré patterns avoiding pitfalls when dealing with real-space-, or reciprocal-space data. We explicitly discuss supported graphene phases, which were characterized by surface x-ray diffraction (SXRD), scanning tunneling microscopy (STM) and low-energy electron diffraction (LEED) and low-energy electron microscopy (LEEM). For the electron diffraction studies, in particular, we point out the intimate relationship between multiple scattering and our generalized method of constructing moiré beating frequencies. The derived results can also be used to identify incommensurate phases and can be easily applied for other related 2-dim systems that evolve moiré patterns.

2. General properties of *n*th-order moiré patterns

Within this section we outline several general properties of hexagonal coincidence phases that determine the appearance of hexagonal moirés. The indexing of commensurate moiré phases is also addressed.

2.1. Simplified notation of commensurate hexagonal moiré patterns

The description of two coinciding hexagonal lattices uses the 120° notation usually chosen in crystallography. Following this notation, the real-space unit cell vectors $\vec{a}_i$ are rotated by 120° with respect to each other and the reciprocal-space vectors $\widetilde{a}_i$ are rotated by 60°, accordingly. Lattice vectors and vectors belonging to the superstructure of a commensurate moiré pattern are defined in real and reciprocal-space as displayed in figure 1.

The real-space vector $\vec{v}_{\text{moiré}} = (m,\ n)$ describes one of the unit cell vectors of the moiré supercell (green cell). Following the 120° notation, the supercell in real-space is characterized by the matrix $M = \begin{pmatrix} m & n \\ -n & m-n \end{pmatrix}$ and in reciprocal-space by the corresponding matrix $\tilde{M} = \frac{1}{m^2 - mn + n^2}\begin{pmatrix} m-n & n \\ -n & m \end{pmatrix}$, which defines the corresponding reciprocal-space moiré vector $\vec{K}_{\text{moiré}}$ and its 60° rotated counterpart of the unit cell. Due to the hexagonal symmetry of the system, unit cells rotated by multiples of 60° may also be chosen and it is sufficient to provide the coordinates of only one unit cell vector. Using this simplified notation, the indexing of a commensurate moiré pattern is given by the coordinate tuple $(m, n)_{\text{TM}}/(r, s)_{\text{g}}$ of this vector relating to the TM- and to the g-lattice, respectively.

2.2. Hexagonal symmetry and indexing of symmetrically equivalent moiré unit cells

Due to the hexagonal symmetry of a commensurate moiré each 60° rotated unit cell vector is also suitable for indexing the unit cell with the simplified notation $(m,\ n)_{\text{TM}}/(r,\ s)_{\text{g}}$. Therefore, we find it useful to provide the coordinates of these six vectors:

$$(m,\ n) \overset{R_{60^\circ}}{\Rightarrow} (m-n,\ m) \overset{R_{60^\circ}}{\Rightarrow} (-n,\ m-n) \overset{R_{60^\circ}}{\Rightarrow} (-m,\ -n) \overset{R_{60^\circ}}{\Rightarrow} (n-m,\ -m) \overset{R_{60^\circ}}{\Rightarrow} (n,\ n-m). \quad (3)$$

Equation (3) relates to unit cell vectors following the 120° notation in real-space. Since in the literature an alternative lattice description is found, which uses a unit cell with lattice vectors $\vec{a}_i$ that are rotated by 60° with respect to each other, we provide formula to convert one indexing type into another in appendix B.

2.3. Clockwise and anticlockwise rotation and the induced mirror symmetry of the moiré pattern

We defined a positive rotation by $+\varphi$ as a counterclockwise rotation (see section 2.1) and the commensurability plots introduced in [11], and the ones shown in this paper relate to this sense of rotation. On reversing the rotational direction towards a clockwise rotation, moirés appear that have mirror symmetry with respect to the ones of anticlockwise rotation. This holds whether or not the moirés are commensurate or incommensurate. In the case of commensurate moirés that are indexed following the simplified unit cell notation, mirror symmetry is obtained when reversing the coordinates of the indexed unit cell vector. As a result, we derive equation (4), which provides the correct indices of the two mirrored moiré cells:

Moiré unit cell upon rotation by $+\ \varphi$ of g- over TM-lattices:	Moiré unit cell upon rotation by $-\ \varphi$ of g- over TM-lattices:
$(m,\ n)_{\mathrm{TM}}/(r,\ s)_{\mathrm{g}}$	$(n,\ m)_{\mathrm{TM}}/(s,\ r)_{\mathrm{g}}$.

(4)

The proof of these two properties is given in appendix C.

2.4. Reciprocal-space positions of the beating frequencies in an *n*th-order moiré pattern

As already outlined in the section 1, the reciprocal-space position of each spatial beating frequency in an *n*th-order moiré pattern is determined by the difference vector $\vec{K}_{\mathrm{moiré}} = \vec{k}_{\mathrm{g}} - \vec{k}_{\mathrm{TM}}$ where $\vec{k}_{\mathrm{g}}$ and $\vec{k}_{\mathrm{TM}}$ are the corresponding spatial frequencies of the adsorbate (g) and support lattices (TM). This situation is sketched in figure 2(a) with $\vec{k}_{\mathrm{TM}} = (1,\ 0)_{\mathrm{TM}}$ and $\vec{k}_{\mathrm{g}} = (0,\ 1)_{\mathrm{g}}$ for a first-order moiré pattern. Instead of formally solving these type of equations, which lead to $\vec{K}_{\mathrm{moiré}}$ and finally to analytic expressions of the *n*th-order moiré beating frequencies, we can also consider their geometrical meaning in reciprocal-space (which is also named k-space in the following). The moiré results from the coincidence of the g- and TM-lattices with the g-lattice counterclockwise rotated by an angle φ with respect to the TM-lattice. When continuously rotating the g-lattice, the corresponding first-order g-lattice frequencies perform a revolving motion in k-space. As a result of the difference construction of $\vec{K}_{\mathrm{moiré}}$, also all spatial frequencies of the moiré pattern except the (0, 0)-spot follow circular trajectories in k-space. While the radius of each circle is determined by the g-lattice constant only, the lateral offset of each circle depends on the involved frequency spots of the TM-lattice. Thus, as also sketched in figure 2(b), all spatial beating frequencies of any first-order moiré follow similar circular trajectories, while the size and position of such circles in k-space varies with the relative lattice constants of the two coinciding lattices. The spatial frequencies that follow the trajectories, and come closest to the (0, 0) spot, lead to the first-order moiré beating frequencies of the pattern.

In the general case of *n*th-order moiré patterns, the number of spatial frequencies in k-space rapidly increases as more and more difference vectors between the spatial frequencies of both lattices occur. The total number of spots N in an *n*th-order moiré pattern is given by

$$N = 1 + 2 \times 6s + (6s)^2 \quad (5)$$

where s is the sum of the orders n in the pattern, i.e. $s = \sum_{i=1}^{n} i$. The first term in equation (3) relates to the (0, 0)-spot, the second term results from the difference vector between the (0, 0)-spot with the remaining $6s$ spots of each lattice (the g- and the TM-lattices) and the last term represents the possible combinations of the $6s$ spots of each lattice. As a result, a first-order moiré pattern contains $1 + 12 + (6)^2 = 49$ spatial frequencies, as explicitly calculated in [11], while already a second-order moiré pattern contains $1 + 36 + (18)^2 = 361$ spots in k-space. Although the pattern of higher-order moirés contains many spots and the trajectories are seemingly much more complex (see also movie SD 1 of the supplementary data), the building principle is the same as for the one of lowest order, except that *n*th-order moiré patterns contain circular trajectories of larger radii. This is sketched in figure 2(c), where the beating frequencies of a second-order moiré pattern follow circular trajectories with radii $\tilde{a}_{\mathrm{g}}$, $\sqrt{3}\ \tilde{a}_{\mathrm{g}}$ and $2\tilde{a}_{\mathrm{g}}$ arising from the revolving motion of the $(1,\ 0)_{\mathrm{g}}$-type, $(1,\ 1)_{\mathrm{g}}$-type and $(2,\ 0)_{\mathrm{g}}$-type spots in reciprocal-space.

During the revolving motion of the g-lattice, several of the k-space spots of a given order n may temporarily approach the (0, 0) beam, generating the *n*th-order moiré beating frequencies, which appear as a large wavelength in the moiré pattern and which have been analytically calculated up to third-order in [11]. If spots approach each other at high symmetry positions in k-space, but do not exactly hit this point, the moiré pattern develops a motif, which may determine the appearance of the moiré pattern, although it does not have translational symmetry with respect to these frequencies. We will discuss such cases in section 3.2. In the case of

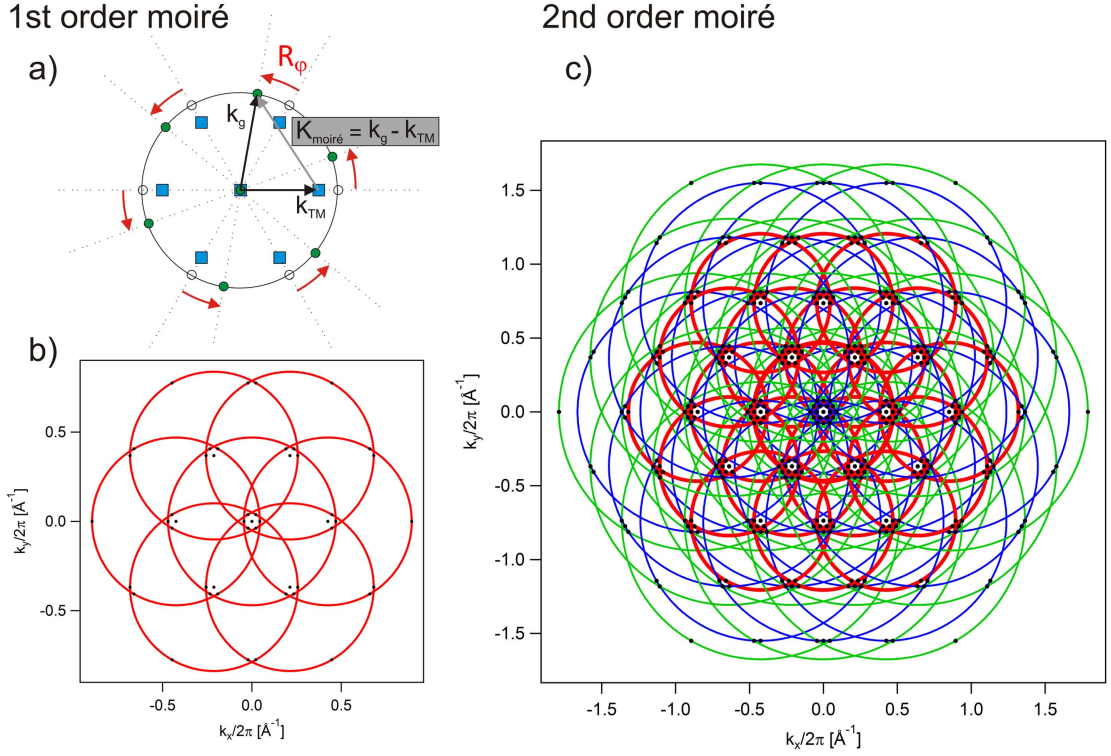

Figure 2. Construction of a spatial beating frequency $\vec{K}_{\text{moiré}}$ in a first-order moiré pattern (a). The resulting trajectories of the beating frequencies in k-space are displayed for a first-order moiré pattern (b) and for a second-order moiré (c). The seemingly more complicated trajectories are formed by the same building principles as the ones of the first moiré, but due to the presence of $(1,\ 0)_{\tilde{g}}$, $(1,\ 1)_{\tilde{g}}$ and $(2,\ 0)_{\tilde{g}}$ spots in the rotating reciprocal lattice of graphene, circular trajectories with radii $\tilde{a}_g$ (red), $\sqrt{3}\ \tilde{a}_g$ (blue) and $2\tilde{a}_g$ (green) appear in the k-space graph. All images were calculated for the parameter $x = a_{TM}/a_g = 1.104$, which applies for g/Ir (111). The small black spots indicate the beating frequency position at a rotation angle of $\varphi = 0°$. An animated version of figure 2(c) is available in supplementary data SD 1.

commensurability, the moiré pattern relates to a unit cell, which arises if the spatial difference frequencies belong to both the g- and the TM-lattices. In order to sort out such cases, we introduced so-called commensurability plots, which visualize the cases where the conditions required for commensurability are fulfilled (see [11]). In the following section, we discuss a method that simplifies this task.

2.5. Commensurability and the moiré cell augmentation method

Instead of trying to identify commensurate moiré phases that host one beat per unit cell, one may also ask whether commensurate multiples of this unit cell exist. The augmentation must be compatible with the hexagonal symmetry of the problem. Possible augmentation factors are 3, 4, 7, 9, 12, 13, 16, … which can be derived from the so-called hexagonal sequence number introduced by Tkachenko [14]. What seems to lead only to redundant cells, provides in fact new solutions of potential commensurate moiré phases. This is best explained for the case of doubling $L_{\text{moiré}}$ (equation (1)) and addressing a quadrupled moiré cell size.

Let us first use the already introduced simplified moiré cell indexing introduced in section 2.1 and apply the results to first-order moirés in order to illustrate the technique of cell augmentation. Referring to a non-augmented unit cell, a commensurate moiré is characterized by the indexing, which is called non-augmented cell indexing in the following:

$$(m,\ n)_{\text{TM}}/(r,\ s)_{\text{g}}. \tag{6}$$

For example, when addressing aligned g- and TM-lattices, the $(11, 0)_{\text{TM}}/(12, 0)_{\text{g}}$ and the $(12, 0)_{\text{TM}}/(13, 0)_{\text{g}}$ moiré phases are two possible first-order moirés, which subsequently increase in size while keeping the commensurability with respect to the two lattices. Note that first-order moirés are of the type $(m,\ n)_{\text{TM}}/(r = m + 1,\ s = n)_{\text{g}}$ as shown in [11]. When instead searching for commensurate quadrupled cells, each unit cell vector is multiplied by a factor of two and the moiré indexing relates to:

$$(\tilde{m},\ \tilde{n})_{\text{TM}}/(\tilde{r},\ \tilde{s})_{\text{g}} = (2m,\ 2n)_{\text{TM}}/(2r,\ 2s)_{\text{g}}. \tag{7}$$

Using this notation for the above example of a first-order moiré and inserting $(m,\ n)_{\text{TM}}/(r = m + 1,\ s = n)_{\text{g}}$ into equation (7), we end up with the quadrupled cell notation as $(\tilde{m},\ \tilde{n})_{\text{TM}}/(\tilde{r},\ \tilde{s})_{\text{g}} = (\tilde{m},\ \tilde{n})_{\text{TM}}/(\tilde{m} + 2,\ \tilde{n})_{\text{g}}$. Thus, the aligned g- and TM-lattices would result in subsequently increasing moiré cells with the notation:

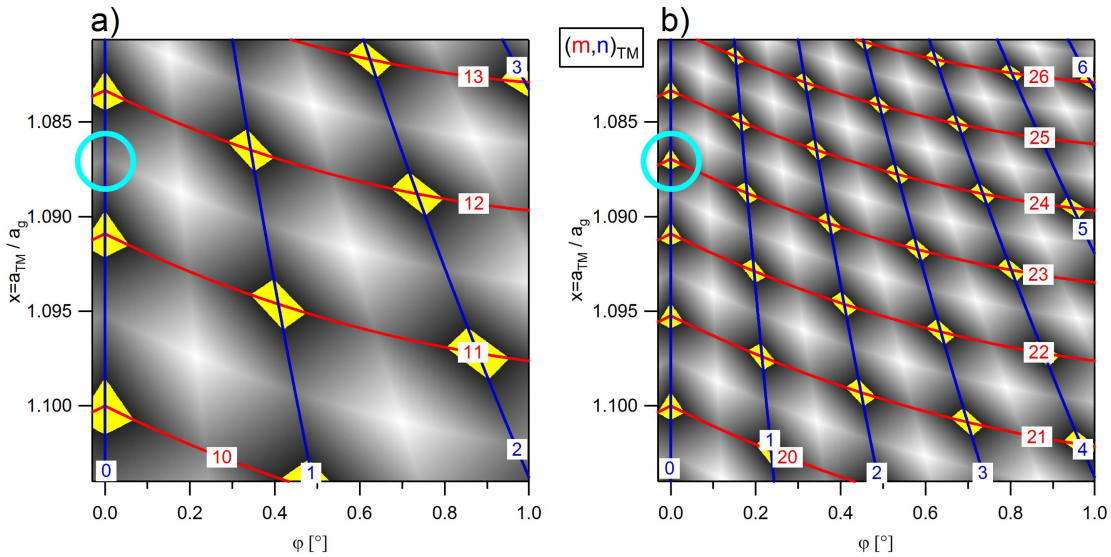

Figure 3. First-order commensurability plots spanning the (x, φ) parameter-space of potential moirés phases of graphene on Ru(0001). (a) Commensurability plot relating to the non-augmented cell notation and (b) relating to a quadrupled moiré cell. It is easily seen that in the augmented cell notation, four times as many commensurate phases appear while every fourth phase is redundant with the ones indicated in figure 3(a). The light blue circles marks the parameter-space where the so-called $(23, 0)_{TM}/(25, 0)_g$ phase is found for the aligned moiré of g/Ru(0001) [25, 26].

$(22, 0)_{TM}/(24, 0)_g$, $(23, 0)_{TM}/(25, 0)_g$ and $(24, 0)_{TM}/(26, 0)_g$. The first and the last cell of this sequence are redundant with respect to the already mentioned non-augmented cells of our example. Instead, the $(23, 0)_{TM}/(25, 0)_g$ moiré indicates a new commensurate phase, which is not identified during the search when using non-augmented cells, since dividing each vector by the augmentation factor two leads to a $(11.5, 0)_{TM}/(12.5, 0)_g$ cell, which obviously does not consist of integer numbers. Although it is obvious that cell augmentation readily leads to large cells, moiré patterns have been identified for supported graphene such as the $(23, 0)_{TM}/(25, 0)_g$ cell reported for graphene on Ru(0001) [25, 26] and the $(19, 1)_{TM}/(21, 1)_g$ moiré found for graphene on Ir(111) [27, 28]. The cell augmentation method is the real-space approach to the description of Artaud *et al*, who discussed the k-space conditions of so-called multiple beatings within a moiré cell [12]. Figures 3(a) and (b) display first-order commensurability plots in non-augmented and quadrupled cell notation for possible moirés of the system g/Ru(0001) at small rotation angles φ of the two lattices.

The vertical axis displays the lattice ratio $x = a_{TM}/a_g$ of the two coinciding lattices while the horizontal axis is the rotation angle φ. As outlined in [11], an nth-order commensurability plot displays the gray scale of a function that indicates how much the nth-order moiré beating frequency deviates from the closest nearby unit cell vector of a commensurate cell within the parameter-space (x, φ) of the moiré. At the local minima the displayed deviation function turns zero, which indicates points in the (x, φ) parameter-space, where commensurability between the graphene and the TM-substrate lattice is met. The points, where such minima appear, are marked by yellow patches in the graph. They occur where the additionally plotted $(m, n)_{TM}$ contour traces (red and blue curves) cross each other. As has been shown in [11], in a first-order commensurability plot the $(r, s)_g$ contour traces that relate to the g-lattice coincide with the $(m, n)_{TM}$ ones. When referring to a non-augmented cell notation, as in figure 3(a), these $(r, s)_g$ indices are calculated as $(r = m + 1, s = n)_g$. According to the indexing introduced in equation (7) for a quadrupled cell, the indices that relate to the graphene lattice are derived from figure 3(b) as $(\tilde{r} = \tilde{m} + 2, \tilde{s} = \tilde{n})_g$. Comparison of figures 3(a) and (b) shows that the quadrupled cell identifies four times as many commensurate phases of the system, while every fourth phase is redundant with the corresponding one found when referring to the non-augmented cell notation. The light blue circle in both plots indicates the parameter-space, which applies for the so-called $(23, 0)_{TM}/(25, 0)_g$ moiré phase of g/Ru (0001) [25, 26]. It is clearly seen that this phase is correctly identified in figure 3(b), which refers to a quadrupled unit cell. Please also note that the identified $(23, 0)_{Ru}/(25, 0)_g$ moiré hosts four beats per unit cell as experimentally observed [25] and also noted by Artaud *et al* [12].

Following the outlined strategy, we can also relate our search to tripled moiré cells, which asks for commensurability with respect to a cell length of $\sqrt{3}\ L_{moiré}$ and an orientation of the unit cell, which is turned by 30° with respect to the non-augmented cell (i.e. a tripled unit cell that is aligned to the so-called $\sqrt{3}$ direction of the hexagonal lattice). In this case, we can use equation (3) to show that simple moiré cells $(m, n)_{TM}/(r, s)_g$ relate to tripled cells with the notation:

$(\tilde{m}, \tilde{n})_{TM} = (m, n)_{TM} + R_{60°}(m, n)_{TM} = (m, n)_{TM} + (m - n, m)_{TM} = (2m - n, m + n)_{TM}$ and

$(\tilde{r},\,\tilde{s})_{\mathrm{g}} = (2r - s,\, r + s)_{\mathrm{g}}$, accordingly. Thus, the moiré indexing is given by

$$(\tilde{m},\,\tilde{n})_{\mathrm{TM}}/(\tilde{r},\,\tilde{s})_{\mathrm{g}} = (2m - n,\, m + n)_{\mathrm{TM}}/(2r - s,\, r + s)_{\mathrm{g}}. \tag{8}$$

Please note that the indexing $(\tilde{m},\,\tilde{n})_{\mathrm{TM}}/(\tilde{r},\,\tilde{s})_{\mathrm{g}}$ relates to the tripled cell notation. Introducing the conditions of a first order moire $(r = m + 1, s = n)$ into equation (8) leads to first order moirés in tripled cell notation as $(\tilde{m},\,\tilde{n})_{\mathrm{TM}}/(\tilde{m} + 2,\,\tilde{n} + 1)_{\mathrm{g}}$. The indexed cells can be easily converted into indexing with respect to the non-augmented cell $(m,\,n)_{\mathrm{TM}}/(r,\,s)_{\mathrm{g}}$ according to:

$$m = (\tilde{m} + \tilde{n})/3,\;\; n = (2\tilde{n} - \tilde{m})/3 \text{ and } r = (\tilde{r} + \tilde{s})/3,\;\; s = (2\tilde{s} - \tilde{r})/3. \tag{9}$$

Now, each third cell is redundant with respect to the identified moiré cell when using the non-augmented cell notation and equation (9) leads to integer numbers (m, n) accordingly. On the other hand, each of the following two cells represents a new solution of potential commensurate phases that are not identified when relating to a non-augmented cell.

2.6. Predicting the commensurability of the $(6\sqrt{3} \times 6\sqrt{3})R_{30^\circ}$ moiré of g/SiC(0001) by applying the moiré cell augmentation method

Calculating commensurability plots for first- and second-order moirés using augmented cells is a very convenient way to derive unit cells without having to include higher-order lattice frequencies. This is discussed for the case of the $(6\sqrt{3} \times 6\sqrt{3})R_{30^\circ}$ moiré with the unit cell notation $(12, 6)_{\mathrm{TM}}/(13, 0)_{\mathrm{g}}$, which is reported for graphene on SiC(0001) [24]. This moiré occurs for a graphene lattice that is turned by 30° with respect to the SiC-lattice and a g-lattice constant so that 13 g-lattice spacings match $6\sqrt{3}$ SiC-lattice units. We can compute the first- and second-order commensurability plot for the parameter-space of this moiré pattern, as shown in figures 4(a) and (b). The left vertical axis of each plot indicates the relative lattice constant $x = a_{\mathrm{SiC}}/a_{\mathrm{g}}$, while the right one displays the absolute graphene lattice constant a_{g} when considering the lattice constant of SiC(0001) $a_{\mathrm{SiC}} = 3.07$ Å. The horizontal axis represents the lattice rotation angle φ and the plots span the region that includes the parameters ($a_{\mathrm{g}} = 2.454$ Å, $x = a_{\mathrm{SiC}}/a_{\mathrm{g}} = 1.251$, $\varphi = 30^\circ$) for which the commensurate moiré with the indexing $(12, 6)_{\mathrm{SiC}}/(13, 0)_{\mathrm{g}}$ is reported [24]. Figures 4(a) and (b) show that in the displayed parameter range no intersection of all four isolines $(m, n)_{\mathrm{TM}}$ and $(r, s)_{\mathrm{g}}$ is found that would indicate the presence of a commensurate phase. In particular, the $(12, 6)_{\mathrm{SiC}}/(13, 0)_{\mathrm{g}}$ phase does not appear. Instead, in figure 4(c) the unit cell is correctly identified at the expected parameter-space. Here, the second-order commensurability plot is computed for a tripled moiré cell, where integer numbers $\widetilde{m}$, $\tilde{n}$ are searched so that $\vec{v}_{\mathrm{moiré}} = (\tilde{m},\,\tilde{n})_{\mathrm{SiC}}$ leads to an augmented cell of $\sqrt{3}\,L_{\mathrm{moirè}}$ cell length, which is 30° rotated with respect to the non-augmented cell. We should point out that commensurability plots directly lead to the graphene lattice strain ε required for commensurability of the identified moiré phases. This is achieved by referencing the predicted graphene lattice constant to the calculated one of free-standing graphene of 2.456 Å at 300 K [29], which is also displayed in figure 4(c). Please note that in figure 4(c) a $(9, 9)_{\mathrm{SiC}}/(13, 7)_{\mathrm{g}}$ commensurate unit cell is also identified, which requires almost the same g-lattice constant as the one in the $(12, 6)_{\mathrm{SiC}}/(13, 0)_{\mathrm{g}}$ moiré phase, but appears at a slightly smaller rotation angle. In contrast to the $(12, 6)_{\mathrm{SiC}}/(13, 0)_{\mathrm{g}}$ moiré, this phase has not been reported so far.

Figures 4(a)–(c) show that we easily find the correct unit cell of the $(12, 6)_{\mathrm{SiC}}/(13, 0)_{\mathrm{g}}$ moiré when using the tripled cell notation, whereas this fails when referring to the non-augmented cell. Why this is the case can be understood when carefully analyzing the spatial beating frequencies that account for the moiré pattern. By constructing the beating frequencies of a second-order moiré as outlined in section 2.4, we can calculate their positions in reciprocal-space for the parameters of the moiré. Figure 4(d) displays the relevant k-space sector of the second-order moiré beating frequencies.

The graph shows the $(0, 0)$ beam, the $(1,0)_{\mathrm{SiC}}$, $(0, 1)_{\mathrm{SiC}}$ and the $(1, 1)_{\mathrm{SiC}}$ spots (black) as well as the $(1,0)_{\mathrm{g}}$ spot (blue). In addition, ten more spatial moiré frequencies $k_1, \ldots, k_{10}$ (red spots) appear according to the construction $\vec{K}_{\mathrm{moiré}} = \vec{k}_{\mathrm{g}} - \vec{k}_{\mathrm{SiC}}$. It is clearly visible that k_1 and k_2 are the shortest k-vectors and account for the longest wavelength beat of the second-order moiré. The linear combinations of these two frequencies fill the displayed k-space entirely (the corresponding grid is sketched by black solid lines) and k_1 and k_2 span a (6×6) superstructure with respect to the SiC-lattice. Due to the fact that the $(1, 0)_{\mathrm{g}}$ spot and the remaining spatial frequencies $k_3, \ldots k_{10}$ do not belong to this grid, k_1 and k_2 do not relate to a commensurate cell.

When instead relating to a real-space unit cell of tripled size, spatial beating frequencies at the reciprocal $\sqrt{3}$ positions of the black grid in k-space are addressed (green crosses). The ones closest to the $(0, 0)$ beam relate to a moiré cell of tripled size in real-space. One of the symmetrically equivalent moiré vectors is indicated as $K_{\mathrm{moiré}}$ in figure 4(d). Since two linear independent $K_{\mathrm{moiré}}$ vectors span a reciprocal lattice (green crosses) that hosts all spatial beating frequencies of the second-order moiré, a commensurate phase results and comparison with figure 4(c) shows that $K_{\mathrm{moiré}}$ relates to the identified $(\tilde{m},\,\tilde{n})_{\mathrm{SiC}}/(\tilde{r},\,\tilde{s})_{\mathrm{g}} = (12,\,6)_{\mathrm{SiC}}/(13,\,0)_{\mathrm{g}}$ real-space cell. We can now easily calculate the corresponding non-augmented cell with the help of equation (9) and identify it as $(m,\,n)_{\mathrm{SiC}}/(r,\,s)_{\mathrm{g}} = (6,\,0)_{\mathrm{SiC}}\Big/\left(\frac{13}{3},\,-\frac{13}{3}\right)_{\mathrm{g}}$. Since non-integer numbers appear, this cell is not identified in

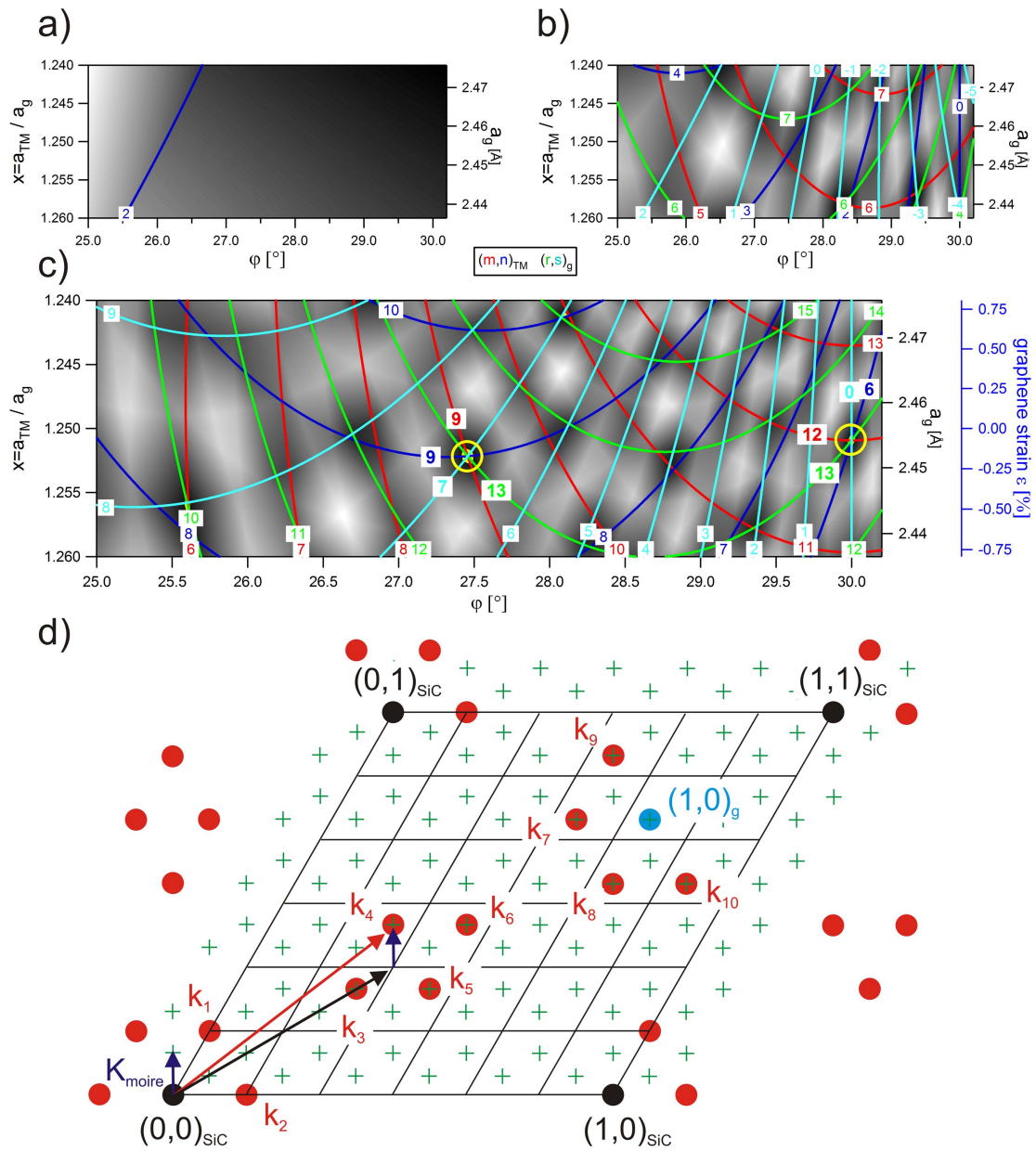

Figure 4. (a) and (b) First-order and second-order commensurability plots relating to a non-augmented moiré cell. (c) Second-order commensurability plot relating to a tripled moiré cell. Two potential commensurate phases are identified. One appears at a rotation angle of 30° (see text). (d) Spatial frequencies of a second-order moiré ($a_{SiC} = 3.07$ Å, $a_g = 2.454$ Å, $\varphi = 30°$) show how relating to the tripled moiré cell refers to spots in k-space (green crosses) at the reciprocal $\sqrt{3}$ positions of the grid, which is spanned by the vectors k_1 and k_2. The vectors closest to the (0, 0) beam refer to the commensurate $(12, 6)_{SiC}/(13, 0)_g$ cell, which is identified in (c). One of the symmetrically equivalent moiré vectors is indicated as $K_{moiré}$.

the corresponding commensurability plot of figure 4(b), while the tripled cell leads to integer numbers and to the identified commensurate cell of the moiré in figure 4(c).

Finally, we can ask, how many orders n have to be considered when wanting to identify the moiré cell in an nth-order commensurability plot while relating to a non-augmented cell. For this purpose, we draw our attention to the other spatial beating frequencies of the second-order moiré pattern in figure 4(d). As has been already noted, k_1 and k_2 and the other beating frequencies $k_3 \ldots k_{10}$ reside on different types of k-space position. The first two reside at intersections of the black grid, all others on positions marked by green crosses, which relate to the $\sqrt{3}$ k-space positions. We can now construct linear combinations of the two types of beating frequency so that they equal $K_{moiré}$ or symmetrically equivalent vectors. In appendix D we list such linear combinations. In addition, we can determine the coordinates of all beating frequencies $k_1 \ldots k_{10}$ according to the building principle of the second-order moiré pattern, which are also listed in appendix D. As a result, we derive the coordinates of the listed linear combinations of the spatial beating frequencies that lead to a symmetrically equivalent vector of $K_{moiré}$. One of the linear combinations is $K_{moiré} = 2(k_1 + k_2)\text{-}k_4$, which is sketched in

figure 4(d). As also shown in appendix D, this linear combination consists of the difference of a reciprocal sixth-order g-lattice and an eighth-order SiC-lattice vector. Since all other linear combinations require equal or higher-order lattice frequencies, $K_{moiré}$ appears as spatial frequency in an nth-order moiré pattern only for $n \geqslant 8$ (see appendix D). Correspondingly, the moiré unit cell cannot be identified in a commensurability plot lower than the eighth-order when relating to a non-augmented moiré cell. The discussed example shows the great simplification of the search for commensurate cells using augmented moiré cells: the $(6\sqrt{3} \times 6\sqrt{3})R_{30°}$ moiré reported for g/SiC(0001) is already correctly identified in a second-order commensurability plot when relating to a tripled moiré cell, while it requires nth-order spatial lattice frequencies with $n \geqslant 8$ in order to find the commensurate cell when referring to a non-augmented moiré cell.

3. Extracting moiré parameters from experimental data

In the following chapter, strategies are outlined how to extract moiré parameters from experimental data. For this purpose, the application of our model is of great use, because it helps to identify the possible commensurate phases of the moiré. As will be shown, a careful frequency analysis also enables the identification of incommensurate phases. We separately discuss the moiré pattern analysis for data sets acquired by different experimental techniques, because each technique has its advantages and short comings which have to be taken into account during the moiré analysis.

3.1. Indexing moiré cells using surface SXRD data

SXRD provides data on surface moiré structures with highest precision in k-space. From the acquired reciprocal-space data the lattice constants and the rotation angle between the two lattices may be extracted. If lateral or vertical atom displacement within the two coinciding lattices occurs, satellite spots appear in the diffraction data, which can be attributed to moiré beating frequencies [25, 26, 30, 31]. On the other hand, when the lattice constants and the orientation of the two lattices are already known precisely, we can use our geometric construction to identify possible commensurate unit cells of the generated moiré that lead to the correct indexing of the moiré.

We show an example of a rotational graphene phase found recently on Ir(111) by Jean *et al* [27]. The authors reported grazing incidence XRD data at 200 K that revealed a g-lattice constant of (2.4521 ± 0.0008) Å and a rotational angle of $(2.37 \pm 0.06)°$ with respect to the Ir-lattice ($a_{Ir} = 2.7129$ Å at 200 K [32]). The reported moiré surface phase can be indexed with the help of the first-order commensurability plot shown in figure 5.

The moiré indexing can be directly seen in the plot when indicating the ratio of the measured lattice constants x and the measured rotation angle φ together with the corresponding experimental error (green). The intersection of the measured values identifies this moiré phase clearly as a $(10, 4)_{Ir}/(11, 4)_g$ unit cell. Originally, the moiré phase cell was erroneously described by the authors as a $(7, 2)_{Ir}/(8, 2)_g$ unit cell [27], but it was corrected at a later stage by applying our analysis [33]. Table 1 lists the extracted values for the two assignments a and b and the experimental data. While the incorrect assignment of a $(7, 2)_{Ir}/(8, 2)_g$ moiré requires a much too small lattice constant for graphene of $a_g = 2.3494$ Å at 200 K (strain $= -4.4\%$), the measured experimental value of 2.4521 Å matches almost perfectly with the required lattice constant of 2.4524 Å for a $(10, 4)_{Ir}/(11, 4)_g$ commensurate cell (strain $= -0.2\%$). Since the same moiré unit cell was also observed at 300 K, the numbers referring to the corresponding Ir-lattice constant of $a_{Ir} = 2.7147$ Å [32] at room temperature are also given in table 1. The calculated graphene lattice constant of the $(10, 4)_{Ir}/(11, 4)_g$ commensurate cell matches the calculated lattice constant of 2.456 Å of free-standing graphene at 300 K [29] (and 2.457 Å at 200 K, respectively) or the reported room temperature value of 2.454 Å of graphene in the g-Ir(111) $R_{0°}$-moiré phase [34].

3.2. Indexing moiré cells using STM data

STM data provide images of the surface in real-space from which the unit cell can be directly derived. Alternatively, one can extract the existing spatial frequencies by a Fourier transform of the image. The advantage of STM data is that local variations in the pattern due to defects or monoatomic steps can be identified, as they induce local rotation, translation or shearing of the graphene lattice above the substrate [35, 36]. The disadvantage is the limited scanning area where high quality images with sufficient lateral resolution may be acquired. Thus, if very large unit cells occur, one cannot easily distinguish between commensurate and incommensurate phases. One more drawback of such data is the fact that STM images usually suffer from thermal drift and piezo creep. While the drift can be accounted for, as long as it leads to a linear expansion or contraction of the acquired image, piezo creep leads to a nonlinear distortion of the image. Thus, extracting lattice constants with a precision better than 10% error is a difficult task. Similar difficulties are faced when determining absolute angles in an STM image. One way around this difficulty is that one may count lattice sites once atomic resolution is obtained and thus avoid measuring absolute numbers. When doing so, one has to take

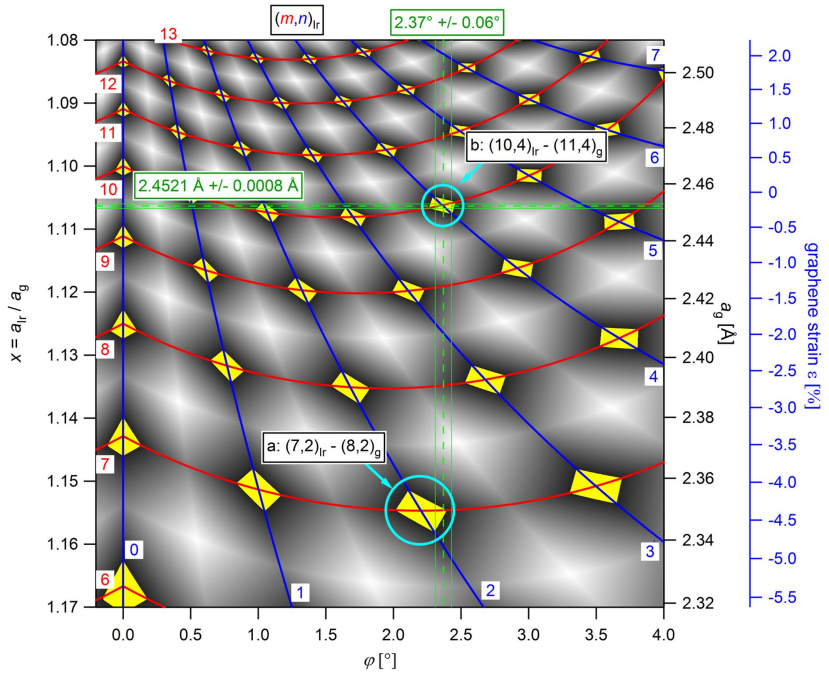

Figure 5. First-order commensurability plot leading to the correct assignment of the (2.37 +/− 0.06)° rotated moiré phase observed by Jean *et al* for g/Ir(111) [27]. The local minima (marked by yellow patches) occur where the additionally plotted $(m, n)_{\mathrm{Ir}}$ contour traces (red and blue curves) cross each other and commensurability of the moiré is met. The indices that relate to the g-lattice are $(r = m + 1, s = n)_{\mathrm{g}}$ (see [11] for details). a: Position of the erroneously assigned $(7, 2)_{\mathrm{Ir}}/(8, 2)_{\mathrm{g}}$ cell in the moiré parameter-space. b: Correctly assigned $(10, 4)_{\mathrm{Ir}}/(11, 4)_{\mathrm{g}}$ moiré cell (see text). The right axis of the graph displays the required graphene lattice constant at 200 K. The additional axis indicates the graphene lattice strain ε with respect to the calculated one of free-standing graphene of 2.457 Å at 200 K.

Table 1. The numbers according to the listed indexing of the moiré cells using; a: incorrect indexing by the authors and b: correct indexing. The Ir-lattice constants are $a_{\mathrm{Ir}} = 2.7147$ Å (300 K) and $a_{\mathrm{Ir}} = 2.7129$ Å (200 K) [27, 32]. The listed values are: T (temperature), a_{g} (graphene lattice constant), $L_{\mathrm{moiré}}$ (length of the moiré unit cell), $\Phi_{\mathrm{moiré,Ir}}$ (rotation of the moiré unit cell with respect to the Ir-lattice), $\Phi_{\mathrm{moiré,g}}$ (rotation of the moiré unit cell with respect to the graphene lattice) and φ (rotation of the graphene lattice with respect to the Ir-lattice).

	Structure	T	a_{g} (Å)	$L_{\mathrm{moiré}}$ (Å)	$\Phi_{\mathrm{moiré,Ir}}$ (°)	$\Phi_{\mathrm{moiré,g}}$ (°)	φ (°)
a	$(7, 2)_{\mathrm{Ir}}/(8, 2)_{\mathrm{g}}$	300 K	2.3510	17.0	16.10	13.90	2.20
		200 K	2.3494	16.9			
b	$(10, 4)_{\mathrm{Ir}}/(11, 4)_{\mathrm{g}}$	300 K	2.4541	23.7	23.41	21.05	2.36
		200 K	2.4524	23.7			
	Experimental data	200 K	2.4521	—	—	—	2.37

into account that the outermost lattice affects the STM image more than the supporting lattice below. Nevertheless, one can derive the moiré parameters by considering that the corrugation in the STM image reflects the convolution of both two lattices as will be shown in the following examples.

In figure 6 we show an STM image of a graphene film on Ir(111) at 300 K after it was grown by catalytic ethylene decomposition (for experimental details see appendix A). Having achieved atomic resolution of the graphene layer, the unit cell of the surface phase can be easily identified as a $(3, 11)_{\mathrm{g}}$ moiré cell by counting lattice sites. The right side of figure 6 displays a similar first-order commensurability plot as the one already shown in figure 5.

Knowing that the indexed $(3, 11)_{\mathrm{g}}$ moiré cell is the mirror of the $(11, 3)_{\mathrm{g}}$ cell according to equation (4), this structure can be identified in the displayed commensurabilty plot. Note that at each intersection of a red (m) and blue contour line (n), a commensurate phase with a $(m, n)_{\mathrm{Ir}}$ unit cell is met. While the indexed cell $(m, n)_{\mathrm{Ir}}$ relates to the Ir-lattice, the cell referring to the graphene lattice amounts to $(r = m + 1, s = n)_{\mathrm{g}}$ for first-order moirés and, thus, the $(10, 3)_{\mathrm{Ir}}/(11, 3)_{\mathrm{g}}$ moiré is easily identified in the right graph of figure 6, as indicated by the green circle. The identified moiré occurs for a graphene layer that is rotated counterclockwise by 1.7° with respect to the underlying Ir-lattice at a lattice constant ratio $x = a_{\mathrm{Ir}}/a_{\mathrm{g}} = 1.108$. We should note that there exists another moiré candidate for a commensurate phase with a $(11, 3)_{\mathrm{g}}$ unit cell vector. In the supplementary data, section SD2, we show that this further candidate appears as a second-order commensurate moiré with a $(10, 7)_{\mathrm{Ir}}/(11, 3)_{\mathrm{g}}$

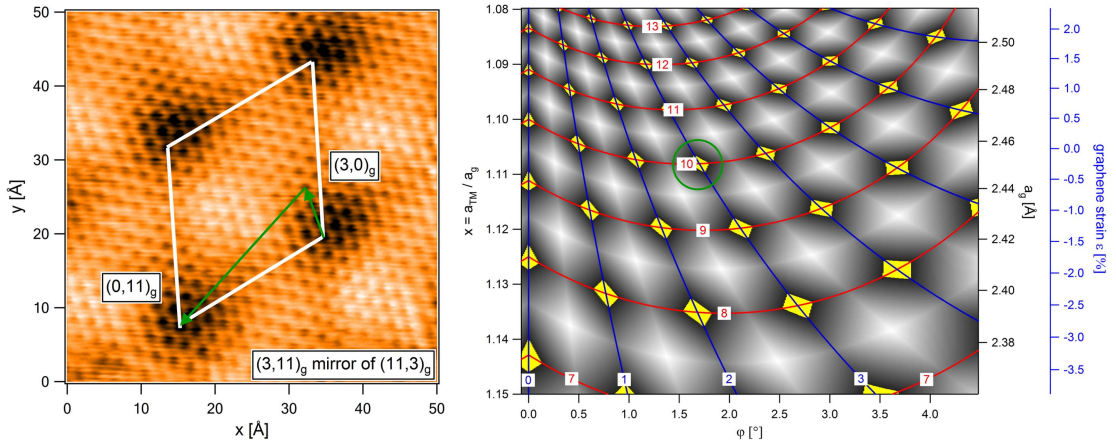

Figure 6. Indexing of the moiré unit cell from an atomically resolved STM image of graphene on Ir(111) at 300 K. Left: the unit cell $(3, 11)_g$ is identified by counting atoms in the atomically resolved graphene layer. Right: the first-order commensurability plot verifies that the identified cell is the mirror of a $(10, 3)_{Ir}/(11, 3)_g$ unit cell relating to a graphene lattice rotated by $-1.7°$ and a graphene lattice constant $a_g = 2.450$ Å. In addition, the lattice strain is indicated (relative to $a_g = 2.456$ Å at 300 K).

unit cell at a rotation angle of 27.7° and $x = 1.108$. Nevertheless, we can exclude this commensurate phase. Since for g/Ir(111) second-order moirés at rotation angles close to 30° are known to contain a strong $(\sqrt{3} \times \sqrt{3})R_{30°}$ motif [11, 23], and since this motif is not visible in the STM image of figure 6, the imaged phase must be a first-order moiré with a $(3, 10)_{Ir}/(3, 11)_g$ unit cell vector as the mirror of the identified $(10, 3)_{Ir}/(11, 3)_g$ moiré in the displayed commensurability plot of figure 6. As a result, the identified moiré appears for a graphene layer with the same lattice constant ratio $x = 1.108$, but a clockwise rotation of $-1.7°$ with respect to the Ir-lattice. Using the known Ir-lattice constant of 2.715 Å at the acquisition temperature of the STM data (300 K), the identified moiré cell indicates a graphene lattice constant of 2.450 Å in the imaged area, i.e. a slightly contracted graphene lattice (by −0.2%) when relating to free-standing graphene at 300 K. This number is much more precise than the one that can be derived from measuring absolute distances in STM images. For example, the moiré unit cell length can be determined from the STM image of figure 6 as (23.6 ± 1.2) Å. Solving equation (1) for the indexed unit cell or simply counting the imaged lattice sites leads to a much less precisely determined graphene lattice constant of (2.4 ± 0.1) Å for the imaged moiré phase. This results in $x = 1.13 \pm 0.05$, which corresponds to a larger vertical axis range than the one of the whole commensurability plot shown in figure 6. The above example shows that moiré patterns enable high-precision measurements whenever distances or angles can be referenced to a lattice with a known structure. Here, the magnifying effect of the length and orientation of moiré frequencies upon slight changes of the parameters of only one of the lattices is of great help. This well-known effect could be used to extract the registry of the lattice along defects such as steps [35, 36] and has even been recently used to address uniaxial stress [12]. When pushing to such limits, care has to be taken, since imaging artifacts produced by the tunneling tip may induce asymmetries that may be misinterpreted. Please also note that the observed $(3, 10)_{Ir}/(3, 11)_g$ moiré pattern is only a slight modification of the $(10, 4)_{Ir}/(11, 4)_g$ pattern observed by Jean *et al* which was discussed in the previous section.

As already mentioned above and outlined in our recent publication [11], graphene films may lead to so-called higher-order moiré patterns. We also showed that moiré patterns may be commensurate with respect to different orders at the same time. This is the case for the so-called $R_{14°}$ moiré observed for g/Ir(111) [23], which is the next example (for experimental details see appendix A). Figure 7 displays an STM image of this phase, its Fourier transform and the corresponding commensurability plots at the lattice rotation angle of interest.

As shown in the commensurability plots, the moiré has a commensurate first- and third-order spatial beating frequency at the same time. Thus, a very robust pattern is expected. The indices given in the commensurability plots indicate that a $(3, 4)_{Ir}/(4, 4)_g$ moiré should occur and indeed the STM image shows a clear (4×4) unit cell (see zoomed image), which also appears clearly in the Fourier transform of the image. The unit cell is not affected by the defect visible within the imaged area (white dots in the upper part of the large STM image). The indexing of a $(3, 4)_{Ir}/(4, 4)_g$ moiré unit cell is in agreement with data in the literature [23]. Again, the commensurability plots provide the parameters x and φ, indicating a slightly compressed graphene lattice (−0.4%) with a lattice constant of 2.447 Å and a graphene layer rotated by $\varphi = 13.89°$ with respect to the Ir(111) lattice. The extracted rotation angle with respect to the Ir-lattice also agrees well with the orientation of the main substrate axis, which is known from oriented step edges of the clean Ir(111) surface (see also [37]). This latter measurement determines the graphene lattice rotation of (15 ± 2)° with respect to the substrate lattice. It represents an absolute number and thus suffers from large errors such as a graphene lattice constant of

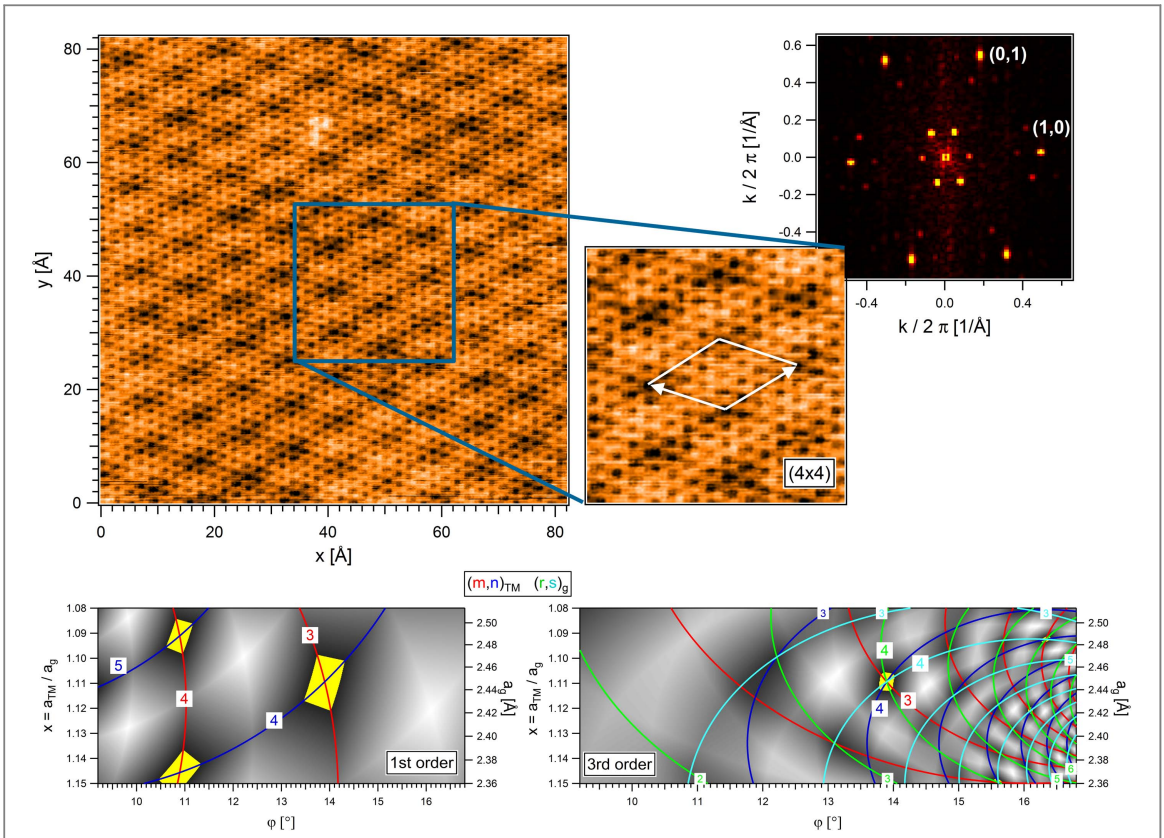

Figure 7. STM image of the R_{14° moiré pattern of graphene on Ir(111). The commensurability plots identify simultaneous commensurability with respect to first- and third-order spatial beating frequencies when rotating the graphene lattice by 13.89° with respect to the Ir-lattice and a graphene lattice constant of 2.447 Å. The commensurate surface phase has a $(3, 4)_{Ir}/(4, 4)_g$ moiré unit cell.

(2.3 ± 0.2) Å directly measured by applying the conversion of the piezo scanners. Using these absolute numbers, a definite indexing of the moiré structure would be not possible.

As a last example, we show STM data of a certain moiré phase that may lead to misinterpretation, since the pattern contains strong, but incommensurate, spatial motif frequencies. Figure 8 displays STM data of g/Ir (111), where the graphene lattice is rotated by about 19° with respect to the substrate lattice (for experimental details see appendix A). From the known lattice orientation of the underlying Ir(111) surface a graphene lattice rotation of (20 ± 2)° and a lattice constant of (2.30 ± 0.15) Å can be deduced. While Loginova *et al* reported a similar pattern on g/Ir(111) with a large commensurate $(13, 5)_{Ir}/(13, 1)_g$ unit cell at a graphene rotation angle of 18.5° [23], close inspection of the STM image in figure 8 reveals a pattern that has no translational symmetry at all within the imaged area.

At a first glance the image shows a pronounced frequency, which relates to a (3 × 3) graphene cell and which is also seen as a pronounced frequency in the Fourier transform of the STM image. On the other hand, close inspection of the zoomed STM image in the right inset of figure 8 shows that true translational symmetry is not given; the dark spots gradually change intensity when moving along the direction of the (3 × 3) cell. Also the moiré pattern reported by Loginova *et al* contained such spatial frequencies, which were called a motif [23]. In our recent publication [11] we explicitly discussed the $(\sqrt{3} \times \sqrt{3})R_{30^\circ}$ motif of the so-called R_{30° moiré found for g/Ir(111) and showed that such a strong motif occurs if several types of beating frequencies approach each other in reciprocal-space at a high symmetry position during the rotation of the g-lattice above the substrate lattice. However, while approaching the high symmetry position, the moiré beating frequencies do not exactly meet. In the displayed moiré of figure 8 the high symmetry points are the $(\sqrt{7} \times \sqrt{7})R_{19^\circ}$ reciprocal-space position of the substrate, which almost coincide with the (3 × 3) position of the graphene layer. True coincidence of these spots in k-space occurs only if the graphene lattice is highly contracted or if the substrate lattice is equivalently expanded. Indeed, a moiré pattern with a commensurate $(2, 3)_{Pt}/(3, 3)_g$ cell is observed for g/Pt(111) [10, 38, 39], because the Pt substrate lattice constant is about 2% larger than the one of Ir [40]. This situation is shown in the upper row panels of figure 9, where all spatial frequencies up to the second-order and their trajectories in k-space are displayed when rotating the graphene lattice from 0° to 19° with respect to the TM-substrate lattice. The upper left chart shows the case for $x = 1.108$ which applies for g/Ir(111), while the upper right chart shows the reciprocal-space frequencies for the moiré at $x = 1.1339$ which applies for g/Pt

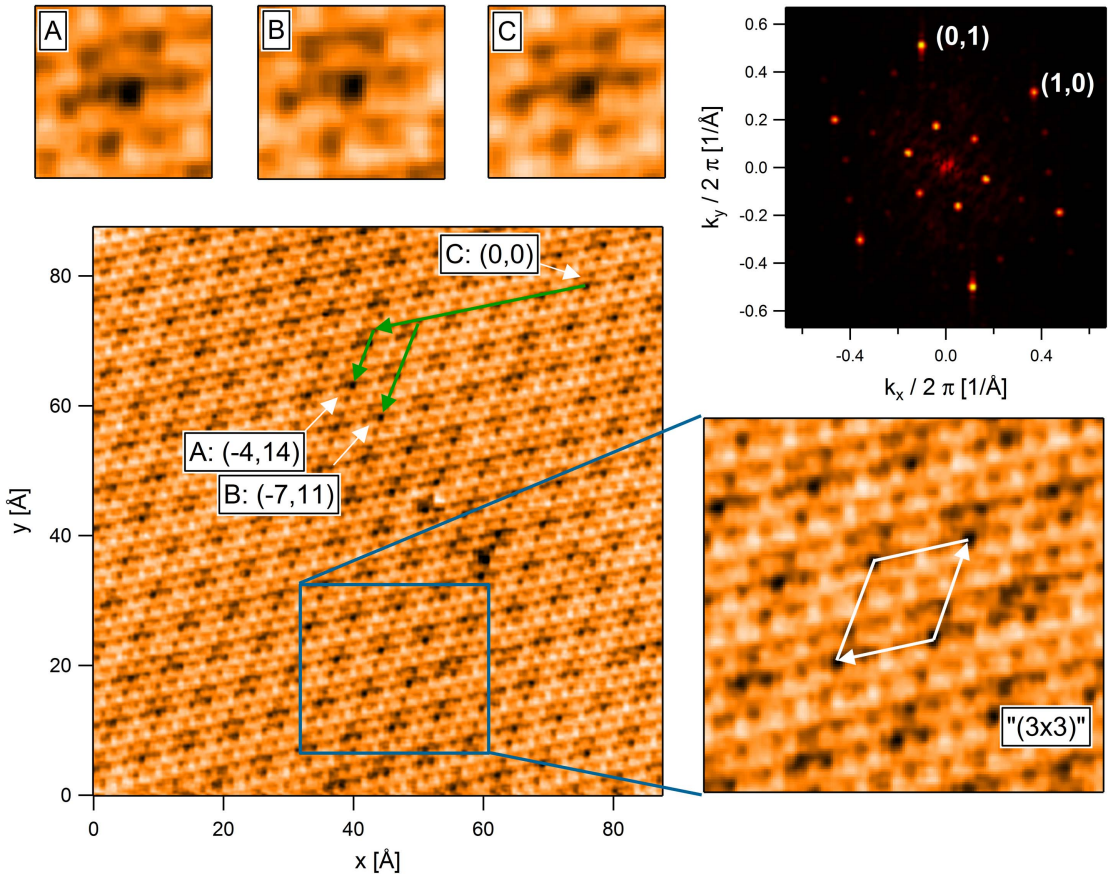

Figure 8. STM image of a moiré pattern found for g/Ir(111) at a graphene rotation angle φ of about 19°. The moiré contains with a strong $(\sqrt{7} \times \sqrt{7})R_{19°Ir}/(3 \times 3)_g$ motif (i.e. almost a $(2, 3)_{Ir}/(3, 3)_g$ moiré unit cell) [37], which appears as a strong frequency in the Fourier transform of the STM image. Nevertheless, zooming in the indicated area reveals that the pattern does not have the translational symmetry of a (3×3) cell. The green vectors in the upper part of the STM image indicate longer translations from one area to another, which are imaged almost identically by STM, as shown in the zoomed areas A, B and C. Close inspection of the STM image also proves that none of these translations strictly repeat within the imaged area (also see figures 9 and 10).

(111). In addition to the $(1 \times 1)_{TM}$ unit cell the reciprocal $\sqrt{7}$ spots are indicated, making it clear why the $R_{19°}$ moiré of g/Pt(111) is commensurate with a $(\sqrt{7} \times \sqrt{7})R_{19°}$-unit cell, while the corresponding moiré of g/Ir (111) only shows a strong motif being incommensurate with respect to this frequency. (In supplementary data SD3, we provide a movie of the spatial beating frequency motion in k-space, which also shows that this situation is reversed for the so-called $R_{14°}$ moiré of the two systems with respect to the $(\sqrt{13} \times \sqrt{13})R_{14°}$-unit cell.) In addition, in the lower row of figure 9, first- and second-order commensurability plots are displayed, proving that, exclusively for g/Pt(111), commensurability exists at a graphene lattice rotation angle of about 19° with respect to first- and second-order at the same time. Commensurability does not exist for any other x within $1.09 < x < 1.15$, although all moirés have a pronounced $(\sqrt{7} \times \sqrt{7})R_{19°}$ motif.

As a result, the moiré pattern imaged in figure 8 does not reflect translational symmetry along the $(\sqrt{7} \times \sqrt{7})R_{19°}$-unit cell direction. On the other hand, the pattern might have translational symmetry with a larger unit cell, where commensurability sets in for moiré frequencies of higher order. In fact, in figure 8 we can identify longer vectors that translate one particular area to another which are almost identically imaged, as shown in the three upper insets A, B and C. We have indicated two such vectors in figure 8, along with the their coordinates $(-4, 14)_g$ and $(-7, 11)_g$. Applying equation (3) shows that these vectors might lead to a $(18, 4)_g$ or a $(18, 7)_g$ moiré unit cell. On the other hand, close inspection of figure 8 verifies that none of the two vectors, or their 60° rotated ones, are repeated twice within the imaged area, so that no commensurate cell can be found. Figure 10 shows why this is the case. Here, we display a third-order commensurability plot of the parameter-space, which applies for g/Ir(111) in the region of interest ($1.101 < x < 1.115$, and $17.5° < \varphi < 19.5°$). Yellow patches indicate where commensurability is possible within the parameter-space. Indeed the patch belonging to the commensurate phase reported by Loginova *et al* with a $(13, 5)_{Ir}/(13, 1)_g$ unit cell is correctly identified [23]. On the other hand, we also indicate the coordinates of the found vectors in figure 8, which would apply to a $(18, 4)_g$ or a $(18, 7)_g$ cell. While we can see that in the imaged area of figure 8 the graphene lattice is substantially more compressed than in the moiré phase reported by Loginova *et al*, we can clearly see that the condition for

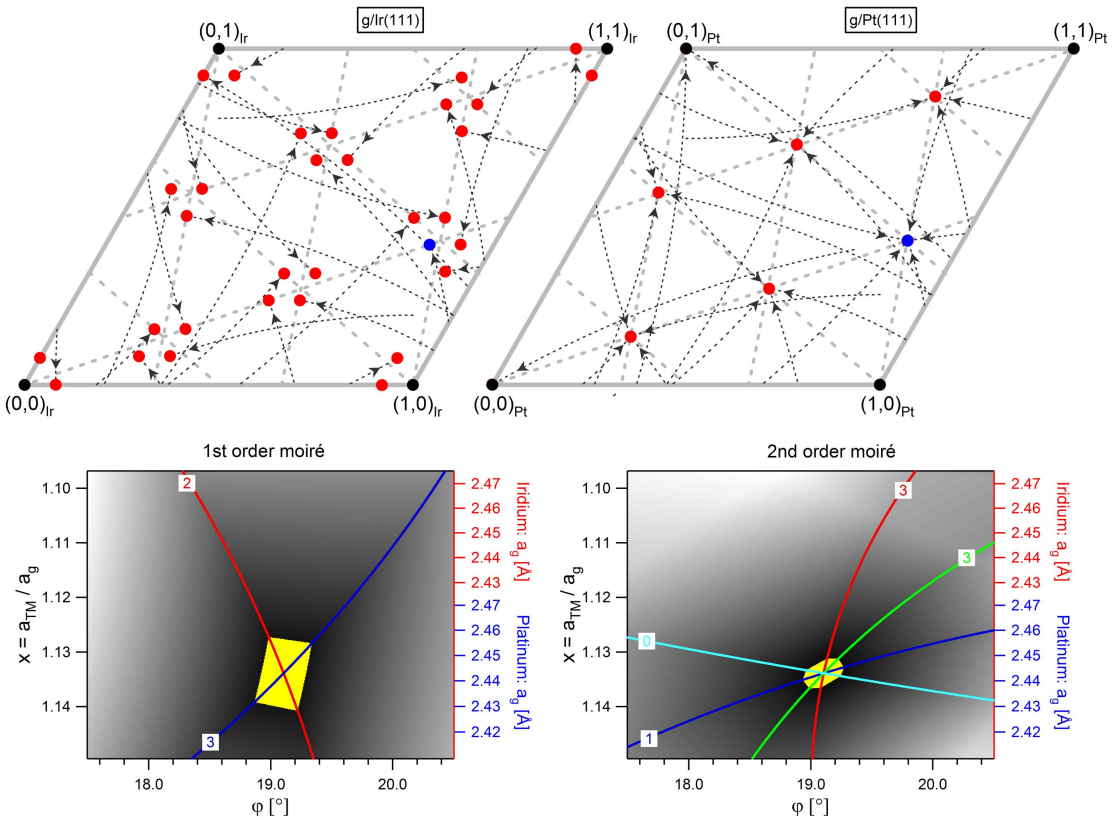

Figure 9. Upper row: trajectories of moiré frequencies in k-space up to second-order for rotation angles close to 19° and $x = 1.1094$ (applying to g/Ir(111)—left chart) and $x = 1.1339$ (g/Pt(111)—right chart). While for g/Pt(111) a commensurate phase is found, g/Ir(111) remains an incommensurate moiré with a strong $(\sqrt{7} \times \sqrt{7})R_{19°}$ motif (the symmetry positions are indicated by dashed lines in light gray). Lower row: first- and second-order commensurability plots prove that only g/Pt(111) leads to a commensurate moiré phase, which is commensurate with respect to first- and second-order frequencies at the same time. An animated version of this figure is provided as supplementary data SD3.

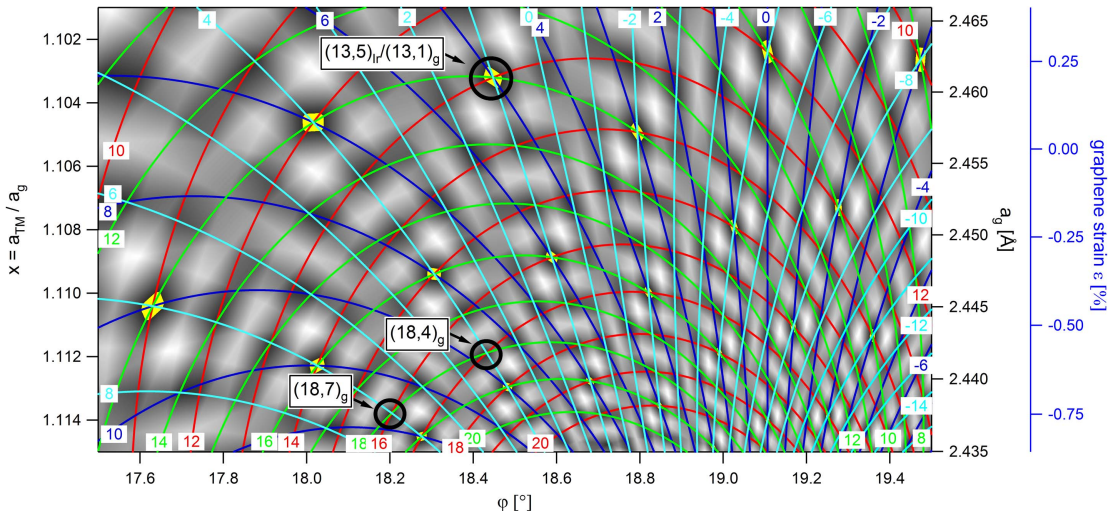

Figure 10. Third-order commensurability plot in the parameter range applying for the $R_{19°}$ moiré of g/Ir(111). While the $(13, 5)_{Ir}/(13, 1)_g$ commensurate phase reported by Loginova *et al* is correctly identified [23], the translation vectors indicated in figure 8 belong to cells that do not lead to commensurate phases.

commensurability, i.e. the crossing of all four curves belonging to the indices $(m, n)_{Ir}$ and $(r, s)_g$, is not fulfilled because one intersection point is always missing. As a result, this approximate translational symmetry is also not given and the imaged pattern is incommensurate.

According to the commensurability plot of figure 10, there are commensurate phases possible in the close vicinity of the $(18, 4)_g$ and $(18, 7)_g$ cells, being $(19, 4)_g$ or $(19, 7)_g$ cells. On the other hand, such cells would lead to the translation vectors $(-4, 15)_g$ and $(-7, 12)_g$, which are not suitable translations when inspecting the STM data of figure 8. Thus, this example shows how sensitive a moiré frequency analysis may be performed. Finally, we should note that STM, being a local probing method, may have difficulties in identifying large unit cells, since one cannot rule out the role of defects, which locally may affect their vicinity such as the two defects visible as dark spots in figure 8.

3.3. Indexing moiré cells using LEED data

LEED may also be used to identify moiré surface phases, although the resolution in k-space is typically inferior with respect to SXRD data. This particularly holds for electron diffraction data that are acquired using LEEM apparatus, since images of the reciprocal plane are readily distorted if the electron beam in the microscope is slightly misaligned with respect to the electron optical axis of the instrument. Another difference of LEED versus XRD is that due to the strong interaction of electrons in solid matter, multiple scattering has to be considered when interpreting LEED data, whereas for (S)XRD single scattering theory applies. X-ray diffraction from two coinciding lattices leads to moiré spots in k-space only if the atoms are vertically and/or laterally displaced from their ideal lattice positions [25, 30]. However, in this case, lattice modulations result in diffraction spots that correspond to the spatial moiré beating frequencies that were discussed in section 2.4. This is not the case for LEED since, due to multiple scattering, a LEED pattern acquired from two coinciding unperturbed lattices already contains diffractions spots that correspond to moiré beating frequencies [30]. While multiple scattering complicates the structure analysis of a moiré by analyzing a so-called LEED I/V experiment [30], one can take advantage of it when extracting the moiré parameters (x, φ) of the surface phase. Knowing that multiple scattering events lead to additional diffraction spots in a LEED pattern that correspond to difference vectors of reciprocal g- and TM-lattice vectors, we note that there is a 1:1 relation of such spots with the predicted moiré beating frequencies, which are calculated as $\vec{K}_{\text{moiré}} = \vec{k}_g - \vec{k}_{TM}$ (see section 2.4). The latter equation may be regarded as double scattering relating to the difference of two reciprocal lattice vectors of a given length. According to our nomenclature, we use the term *n*th-order spatial frequency to express the length of the involved k-vectors in units of the Brillouin zone. We note that triple or other multiple scattering may also always be formally reduced to the difference of two k-space vectors, because one can always calculate one difference vector for each scattering event at a time and subtract the result from the k-space vector that corresponds to the subsequent scattering event. The only difference with respect to double scattering is that the involved k-space vectors may subsequently increase in length, which requires including higher-order beating frequencies of the *n*th-order moiré pattern according to our nomenclature. We should point out that this resemblance addresses the k-space position but not the intensity of the spots. Man and Altman used the described 1:1 relation for first-order moiré diffraction spots in order to analyze minor variations of the lattice alignment of chemical vapor deposited (CVD) graphene with respect to the Ru(0001) substrate in a LEEM experiment, achieving a spatial resolution within the several nm range [41]. In this analysis, the approximately ten-fold augmented rotation of first-order moiré spatial frequencies with respect to the rotation of the graphene lattice versus the Ru(0001) substrate allowed to precisely determine the orientation of the supported graphene layer.

A similar case is given for monolayer graphene on Cu(111). Figures 11(a) and (b) display the LEED data that were were recorded from a Cu(111) facet of a polycrystalline Cu foil on which monolayer graphene was grown by CVD (see appendix A for experimental details). The data were acquired using the SPELEEM instrument of the nanospectroscopy beamline at the ELETTRA synchrotron facility [42, 43]. Polycrystalline Cu foils generally undergo faceting upon CVD growth of graphene [44–46]. As a result, LEED patterns recorded from such surfaces show diffraction spots of two or more inclined surfaces at the same time. When investigating such a system with a LEEM apparatus, one usually aligns the optical axis of the instrument parallel to the surface normal of one of these surfaces. Due to the properties of a LEEM microscope, the diffraction spots emerging from the aligned surface do not move in the reciprocal-space plane when changing the electron kinetic energy, in contrast to diffracted electron beams that are reflected from inclined surface planes. Thus, when recording a set of LEED images as a function of the electron kinetic energy (a so-called LEED *I/V* data set) and summing all images, LEED spots originating from the aligned surface facet become intense, while the ones belonging to the inclined facets are distributed along much less intensive stripes [45, 47]. Applying this trick, one can extract the LEED pattern corresponding to one single facet plane of the faceted polycrystalline Cu foil, which is the Cu(111) plane in our case. Each of the LEED images shown in this section are generated by the described summation procedure. Similar to the study of g/Ru(0001) by Man and Altman [41], we can analyze the LEED pattern of monolayer graphene phases on the Cu(111) facet and precisely determine the rotational alignment of the graphene layer. This can be achieved by measuring the rotational orientation of the first-order moiré beating

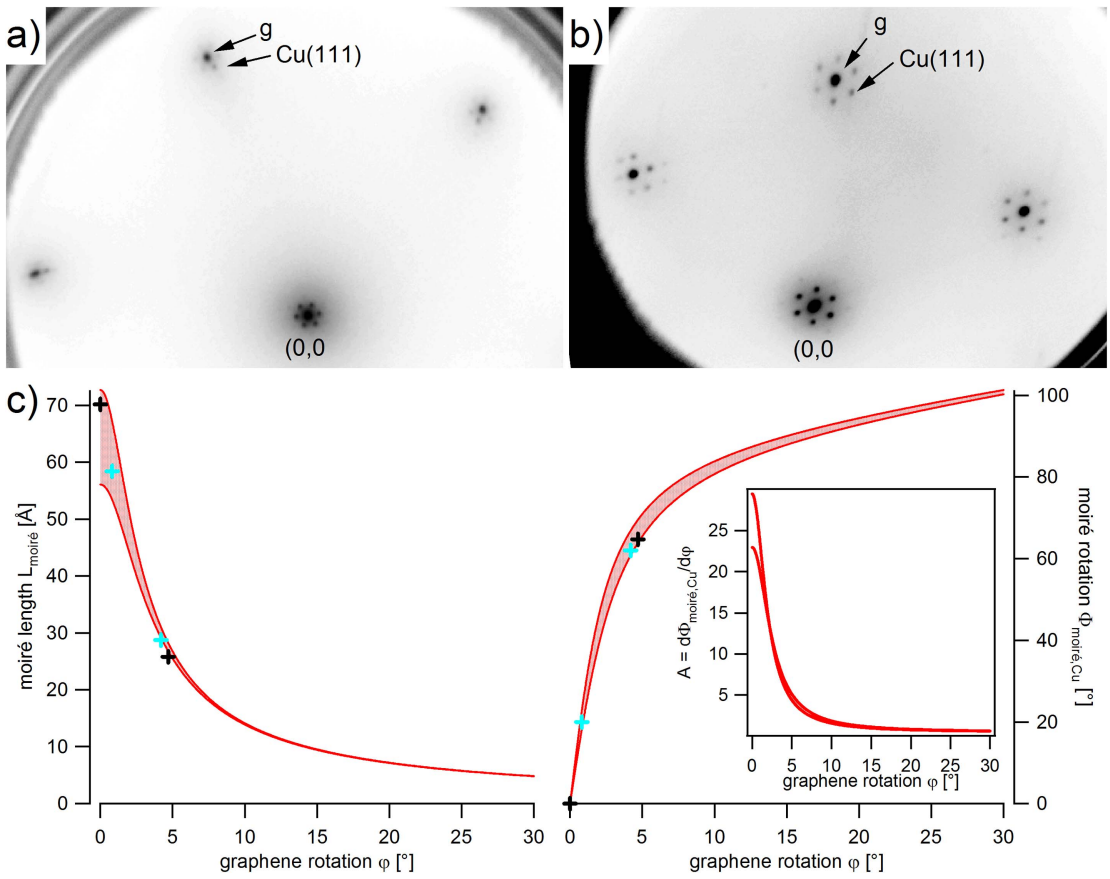

Figure 11. (a) and (b) LEED patterns acquired from two slightly rotated CVD grown graphene phases on a Cu(111) surface of a faceted polycrystalline Cu foil. The patterns were generated by summing LEED patterns of a LEED I/V data set between 50 and 80 eV (see text). (c) Predicted moiré length $L_{\text{moiré}}(\varphi)$ and rotation angle $\Phi_{\text{moiré,Cu}}(\varphi)$ for graphene on Cu(111). The displayed curves relate to a $\pm 0.5\%$ strained graphene layer. The derivative of the $\Phi_{\text{moiré,Cu}}(\varphi)$ curve shown in the inset indicates the moiré rotation enhancement of up to a factor $A = 25$. Light blue crosses mark the moiré length and orientation of the two moiré phases belonging to the LEED patterns shown in (a) and (b). The black data points resemble the corrected assignment of moirés reported in a STM study of g/Cu (111) [48] (see text).

spots and the fact that first-order moiré spots perform an augmented rotation $\Phi_{\text{moiré,Cu}} = A \times \varphi$ in k-space if the graphene lattice is rotated by an angle φ with respect to the underlying Cu(111) lattice. Figure 11(c) displays the predicted moiré length $L_{\text{moiré}}$ and rotation angle $\Phi_{\text{moiré,Cu}}$ for unstrained and slightly strained ($\pm 0.5\%$) graphene on Cu(111). The highly amplified rotation $\Phi_{\text{moiré,Cu}}$ of the moiré pattern is reflected in the very steep $\Phi_{\text{moiré,Cu}}(\varphi)$ curve for small lattice rotation angles φ. Here, amplification factors A up to 25 are reached, as indicated by the derivative of the $\Phi_{\text{moiré,Cu}}(\varphi)$ curve, which is displayed in the inset of figure 11(c). As we will show in the following, due to this large amplification factor the rotational alignment of the graphene layer on the Cu(111) substrate can be determined with high precision. On the other hand, the high amplification A also leads to possible misinterpretation of moiré data, as will also be discussed further below.

By extracting the k-space position of the first-order moiré spots and converting them into real-space vectors, we can calculate the wavelength $L_{\text{moiré}}$ and the orientation $\Phi_{\text{moiré,Cu}}$ of the first-order moiré beating frequency. Additionally, we derive the moiré parameters $x = a_{\text{Cu}}/a_{\text{g}}$ and φ by locating the $(1,0)_{\text{g}}$ and $(1,0)_{\text{Cu}}$ spots in the LEED patterns of figures 11(a) and (b). The extracted data suffer from errors due to distortions of the acquired LEED patterns. Such distortions could not be avoided during acquisition of the diffraction data with the LEEM instrument, because the used Cu foils were non-planar on the 100 μm length scale. As a result, the electrical field inhomogeneity in front of the sample surface induced distortions in the reciprocal image plane, which could not be completely removed when aligning the microscope. Taking into account such errors by analyzing the displayed LEED data while averaging over the symmetrically equivalent diffractions spots, we extract the moiré parameters of the two moiré phases of figure 11 and list them in table 2. For comparison, we also list assigned moiré phases of the g/Cu(111) system reported by Lim *et al* [48], which have to be reinterpreted according to our analysis, as will be discussed further below.

The determined (x, φ) moiré parameters corresponding to the LEED data of figures 11(a) and (b) lead to $L_{\text{moiré}}$ and $\Phi_{\text{moiré,Cu}}$ values, which are listed in table 2, and are also added to the $L_{\text{moiré}}$ and $\Phi_{\text{moiré,Cu}}$ plots of figure 11(c) as light blue crosses. The extracted parameters fit well to the predicted curves for supported

Table 2. Extracted moiré parameters of first-order moirés found for small rotation angles φ of CVD grown graphene on Cu(111), together with the required lattice strain ε with respect to the lattice constant of 2.456 Å at 300 K of free-standing graphene [29]. The upper two rows list the extracted LEED data of figure 11. The data are compared with the incorrect and corrected assignment of atomically resolved STM data from Lim *et al* on g/Cu(111) [48] (see text).

Moiré	$x = a_{Cu}/a_g$ (*)	φ	ε (%)	$\Phi_{moiré,Cu}$	$\Phi_{moiré,g}$	$L_{moiré}$ (Å)
Figure 11(a)	1.041 ± 0.001	$0.8° \pm 0.2°$	-0.07 ± 0.15	$20.0° \pm 3.0°$	$19.2° \pm 3.2°$	61 ± 4 (*)
Figure 11(b)	1.044 ± 0.004	$4.2° \pm 0.3°$	-0.35 ± 0.40	$62.2° \pm 0.8°$	$58.2° \pm 1.1°$	31 ± 3 (*)
Incompatible moiré cell assignment by Lim *et al* [48]						
$(10,0)_{Cu}/(11,0)_g$	1.100	0.0°	−5.4	0.0°	0.0°	25.8 (**)
$(27,0)_{Cu}/(29,0)_g$	1.074	0.0°	−3.1	0.0°	0.0°	70.2 (**)
Corrected assignment of the moiré cells						
$(10,11)_{Cu}/(11,11)_g$ (see text)	1.045	4.7°	−0.4	64.7°	60.0°	25.8 (**)
$(28,0)_{Cu}/(29,0)_g$ (see text)	1.036 (*) (**)	0.0°	+0.4	0.0°	0.0°	70.2 (**)

(*) The data relate to a lattice constant of Cu(111) of 2.555 Å [49].

(**) Experimental data were extracted directly from STM images [48].

graphene, which is strained by less than 0.5%. Indeed, as is also listed in table 2, the two moirés require a slight compression of the graphene lattice by about −0.1% and −0.4%, respectively. We can now discuss these data using the corresponding first-order commensurability plots that characterize the system g/Cu(111). These plots are shown in figure 12.

Figure 12(a) displays the first-order commensurability plot that covers the parameter range of the moiré shown in figure 11(a) with a 0.8° rotated graphene layer on top of Cu(111). Figure 12(b) shows the corresponding charts relating to the moiré of figure 11(b), which results from a 4.2° rotated graphene layer on top of the Cu(111) support. The light blue boxes indicate the (x, φ) parameter range as it has been determined by using the $(1,0)_g$ and $(1,0)_{Cu}$ spots of the two diffraction patterns. In both cases the knowledge on the moiré pattern rotation angle $\Phi_{moiré,Cu}$ allows us to restrict the possible parameter range of the identified moiré phase. This is shown in the magnified plots in the right part of figure 12 where the lines of constant $\Phi_{moiré,Cu}$ are indicated in green for the listed values of table 2. The fact that the rotational alignment of the graphene layer can be measured with high-precision stems from the fact that the moiré performs a highly augmented revolution if the graphene lattice is slightly rotated. This is caused by the almost equal lattice constants of the graphene and the Cu(111) lattice. On the other hand, due to the same reason, a large variety of commensurate first-order moiré phases are possible for slightly rotated graphene on top of Cu(111). As a result, we cannot decide whether the identified moiré phases in figures 11(a) and (b) are commensurate or not within the uncertainty of the experimental data. Even within the restricted parameter-space, the 0.8° rotated graphene may generate a commensurate moiré with a $(26,8)_{Cu}$, a $(26,9)_{Cu}$ or a $(26,10)_{Cu}$ cell. In the case of the 4.2° rotated graphene layer, no commensurate cell is met within the possible moiré parameter range. Therefore, this moiré has to be assigned to an incommensurate phase when relating to a non-augmented moiré cell. When instead referencing a four-fold augmented cell, the magnified commensurability plot indicates that four commensurate phases are possible (see also section 2.5). For example, the intersection of the green dashed line with the red $m = 11$ isoline in the magnified graph relates to a nominal cell size of $(11, 11.5)_{Cu}$. Thus, this potential incommensurate phase would then lead to a commensurate $(22,23)_{Cu}/(24,23)_g$ moiré with four beats within the augmented cell.

Another property of the 4.2° rotated graphene moiré phase should be pointed out. As indicated in table 2, this phase leads to a first-order moiré cell with $\Phi_{moiré,Cu} = 62.2° \pm 0.8°$ and with $\Phi_{moiré,g} = 58.2° \pm 1.1°$, respectively. Due to the highly amplified revolution of the moiré cell, a slight further rotation of the graphene layer causes a moiré pattern that is aligned with respect to the graphene lattice. Thus, a moiré cell aligned with respect to the graphene lattice does not necessarily indicate that the graphene layer is aligned with respect to the substrate lattice. In the case of g/Cu(111) this situation is already reached at very small rotation angles φ, a fact that was overlooked by Lim *et al* who imaged several aligned moiré phases on g/Cu(111) by STM [48]. From atomically resolved STM images the authors deduced two moirés with wavelengths of 25.8 Å and 70.2 Å, respectively. Assuming that the imaged phases originated from a graphene lattice aligned to the Cu(111) support, the authors extracted the graphene lattice constant from the detected moiré wavelength $L_{moiré}$ and assigned the moirés to a $(10,0)_{Cu}/(11,0)_g$ and a $(27,0)_{Cu}/(29,0)_g$ cell, as listed in table 2. This assignment requires unreasonably highly contracted graphene lattices with $\varepsilon = -5.5\%$ and $\varepsilon = -3.1\%$ and the data have to be reinterpreted. The above mentioned possibility of two graphene lattice orientations (aligned and slightly rotated) that result in the appearance of an aligned moiré cell resolves the incorrect assignment of the $(10,0)_{Cu}/(11,0)_g$ moiré cell. At $\varphi = 4.7°$ a $(10,11)_{Cu}/(11,11)_g$ moiré cell appears in the commensurability plot of figure 12(b) requiring an almost unstrained graphene lattice with $\varepsilon = -0.4\%$. The corresponding moiré cell

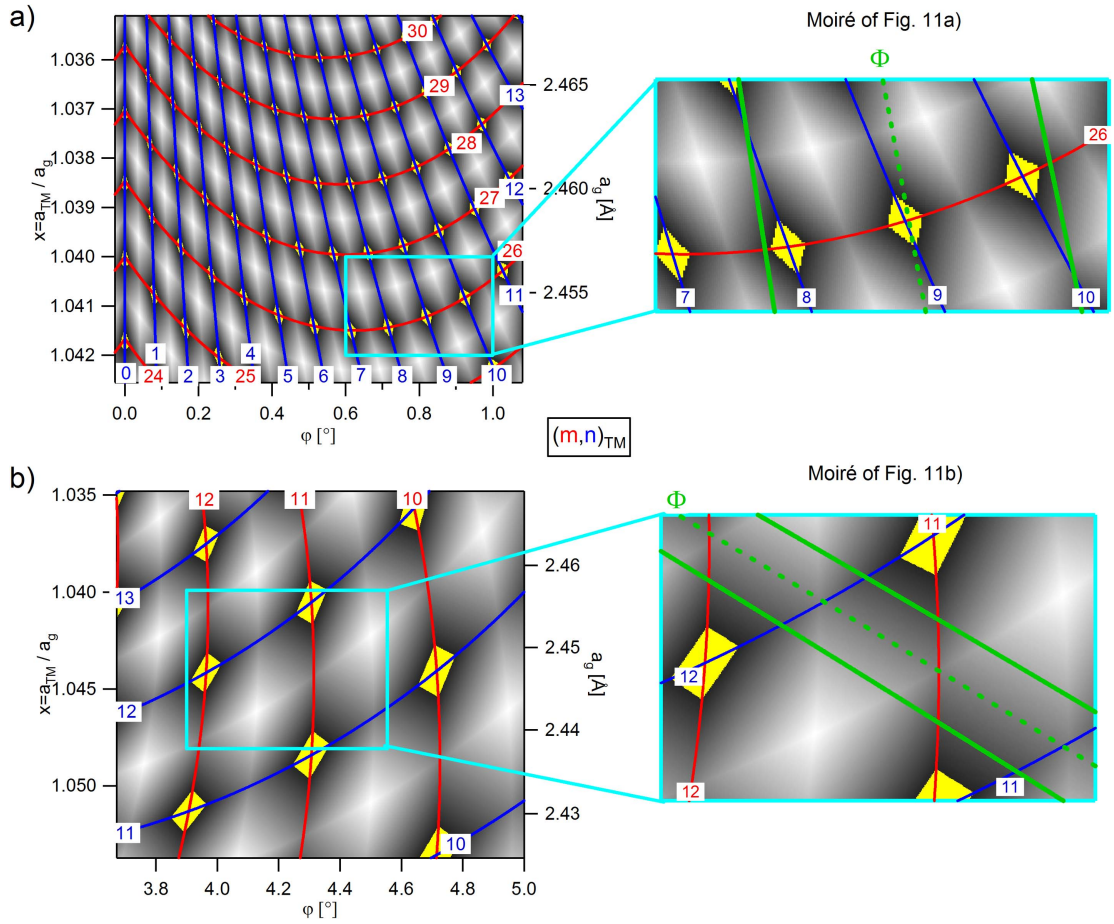

Figure 12. First-order commensurability plots indicating possible moirés of the g/Cu(111) system for graphene lattice rotation angles of (a) $0° \leqslant \varphi \leqslant 1.1°$ and (b) $3.7° \leqslant \varphi \leqslant 5.0°$. The light blue squares in the left charts indicate the determined moiré parameter-space from the analysis of the $(1,0)_g$ and the $(1,0)_{Cu}$ spots of the LEED pattern shown in figures 11(a) and (b). The analysis of the first-order satellite diffraction spots allows us to determine the quantity $\Phi_{moiré,Cu}$. Adding the isolines for constant $\Phi_{moiré,Cu}$ in the magnified commensurability plots (green lines displayed in the right charts) allows us to narrow the parameter-space of possible moirés (see text).

of this phase is turned by 60° (see table 2) and is thus aligned with respect to graphene lattice in accordance with the atomically resolved data of Lim *et al* [48]. The slight misalignment of the moiré with respect to the Cu lattice by 4.7° cannot be detected by STM if the graphene and the Cu(111) lattice are not imaged within the same image. Since this was not the case in the STM study of Lim *et al* (see also discussion in section 3.2), we conclude that the imaged moiré phase must have a cell size close to the mentioned $(10,11)_{Cu}/(11,11)_g$ cell. Our assignment also agrees with the measured value for $L_{moiré} = 25.8$ Å, as can be directly seen by the black crosses in the corresponding graph of figure 11(c).

We should note that Lim *et al* also reported on further phases which were not atomically resolved. Since in such cases all extracted data from the STM images suffer from large errors and one cannot easily derive the moiré parameters x and φ and only speculate on potential commensurate moiré cells. On the other hand, the authors of [48] deduced a commensurate $(27,0)_{Cu}/(29,0)_g$ moiré cell for the surface phase where the 70.2 Å beating frequency was resolved together with atomic resolution of the graphene lattice. In section 2.5 we showed that such a moiré with the cell type $(m,n)_{Cu}/(r = m+2, s = n,)_g$ exists only for first-order moirés when referring to a quadrupled cell, i.e. the unit cell should host four beats. Since the recorded STM image shows a cell with a simple beat only, the proposed unit cell violates the properties of first-order moirés and cannot be correct. Instead, the reported moiré may or may not be commensurate resulting from an aligned graphene lattice with $\varphi = 0°$ and a moiré beat close to a $(28,0)_{Cu}/(29,0)_g$ cell. In this case the assignment would require again an almost unstrained graphene lattice with $\varepsilon = +0.4\%$. Again, figure 11(c) also indicates the consistency of our assignment. All in all, we can summarize that care has to be taken when analyzing moiré phases, where a highly amplified rotation of the moiré cell appears. Also, the assignment of potential commensurate cells has to be done in agreement with the general properties of moiré patterns. The presented example of the LEED data analysis on moiré patterns at small rotation angles between the g- and Cu(111)-lattice shows how the relevant moiré parameters can be consistently extracted.

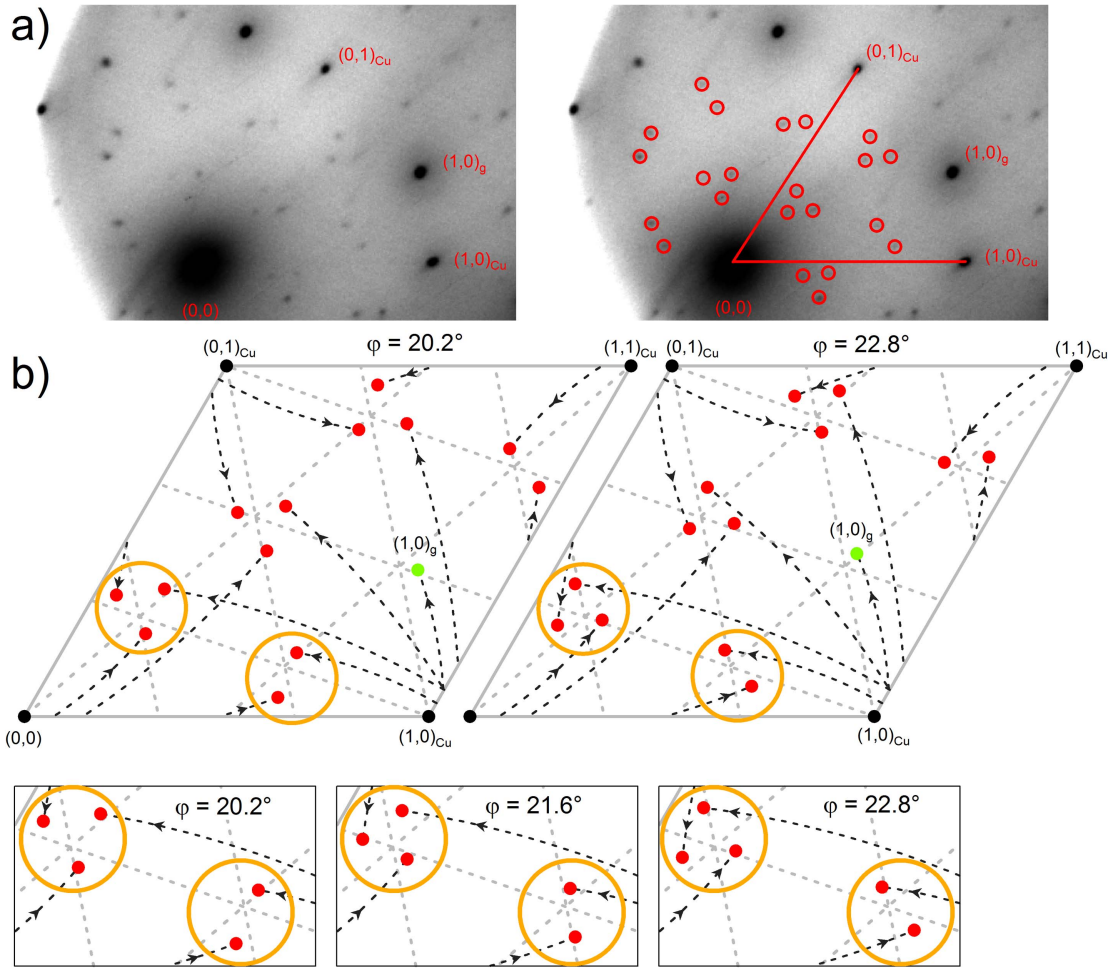

Figure 13. (a) LEED pattern of an approximately 20° rotated graphene layer on Cu(111). In addition to the LEED pattern, the right chart displays the predicted k-space positions of diffraction spots resulting from electron double scattering, which coincide with the calculated second-order moiré beating frequencies of 22.8° rotated graphene on Cu(111). (b) Upper row: calculated spatial second-order frequencies for $x = 1.038$ and $\varphi = 20.2°$ and 22.8° with their trajectories in k-space. Orange circles mark positions close to the ones of the $(\sqrt{7} \times \sqrt{7})R_{19°}$ cell (see dashed lines in light gray), where triple and double spots meet in k-space during the graphene lattice rotation. The augmented rotation of such spots with respect to their center of mass shown in the lower panel can be used to precisely determine the lattice orientation of the graphene lattice on the Cu(111) support (see text). An animated version of this figure is provided as supplementary data SD4.

The concept of LEED data analysis has to be changed when wanting to precisely identify moiré phases caused by highly rotated graphene on Cu(111). As seen in figure 11(c), at a graphene lattice rotation φ between 5° and 10°, the moiré cell revolution of the first-order moiré starts to level off and finally reaches an angle $\Phi_{\text{moiré,Cu}}$ of about 100°. Also the moiré length does not change dramatically, when exceeding rotation angles of the graphene lattice of about 10°. Thus when dealing with highly rotated graphene layers, we cannot exclusively address first-order moiré spots in k-space for the extraction of high-precision data since no amplification effects can be used to restrict the parameter-space of the g/Cu(111) moiré. As already pointed out, the close relation of a LEED pattern and the construction of spatially beating frequencies of a moiré pattern enables us to use higher-order spots for this purpose. Figure 13(a) shows the LEED pattern of monolayer graphene rotated by about 23° with respect to the Cu(111) surface of the faceted Cu foil on which the graphene layer was grown by CVD (see appendix A for experimental details). Similar to the LEED data shown in figures 11(a) and (b), the displayed LEED pattern was generated by summing the LEED images of an I/V data set between 70 eV and 170 eV so that diffraction spots belonging to the aligned Cu(111) surface are intense, while all other ones belonging to inclined Cu facets are distributed into faint lines in k-space, which accounts for the streaky appearance of parts of the displayed LEED pattern.

The left part of figure 13(a) displays the LEED pattern and the position of the (0, 0) spot, the $(1, 0)_{\text{Cu}}$ spots of the Cu(111)-lattice and the corresponding $(1, 0)_{\text{g}}$ spots of the g-lattice. The right part of figure 13(a) repeats the LEED pattern together with all the spatial beating frequencies of a second-order moiré that corresponds to a 22.8° rotated graphene layer on Cu(111). Figure 13(b) displays these beating frequencies for rotation angles of $\varphi = 20.2°$ and 22.8° together with their calculated trajectories in k-space (see section 2.4). Two orange circles

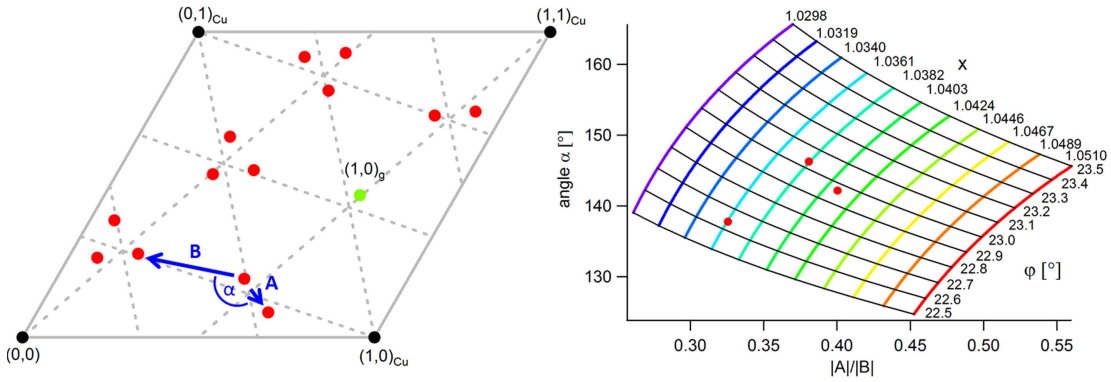

Figure 14. Extraction of the (x, φ) parameters of the moiré shown in figure 13. For practical reasons, the parameters A, B and α were extracted from the LEED image and compared with the predicted values from the second-order moiré frequencies. Three symmetrically equivalent positions were analyzed and resulted in three different positions of the moiré parameter-space, as shown in the right chart. The data scattering is caused by a slight distortion of the LEED image and define the error of the extracted moiré parameters: $\varphi = 22.8° \pm 0.2°$ and $x = 1.038 \pm 0.002$.

indicate k-space positions close to the ones of the $(\sqrt{7} \times \sqrt{7})R_{19°}$ unit cell (see dashed lines in light gray). Here two and, respectively, three beating frequencies meet when approaching a graphene lattice rotation angle of $\varphi = 21.8°$ followed by a separation of the respective spots at larger φ. These triple and double spots perform a quasi-rotation around their center of mass, if the graphene layer is rotated with respect to the Cu(111) lattice (see also the animated movie SD4 in the supplementary data). In the lowest row of figure 13 the orientation of the triple and double spots is indicated for rotation angles $\varphi = 20.2°$, $21.6°$ and $22.8°$. While the graphene lattice rotates only by $2.6°$, the triple and double spots rotate by about $60°$. This highly magnified revolution can be used to precisely determine the orientation of the graphene layer. This is indicated by the red circles in figure 13(a), which mark the coincidence of the experimentally observed diffraction spots with the predicted second-order moiré frequencies of the $22.8°$ rotated graphene layer sketched in figure 13(b).

In order to precisely determine the orientation of the graphene layer, we have to consider the effect of the second moiré parameter x, which also affects the diffraction spot position and which has to be extracted at highest possible precision. The corresponding analysis is shown in figure 14. For practical reasons we did not calculate the rotation angle of the triple and double spots around their center of mass, because some of the LEED spots are very weak. Instead, we determined the parameters A, B, and α of the indicated spots in the left graph of figure 14. Extracting these numbers from three symmetrically equivalent positions of the experimental LEED pattern and comparison with the predicted ones within the parameter-space (x, φ) of the moiré leads to the right chart of figure 14.

Although the data extracted from the three symmetrically equivalent positions should lead to the same spot in the moiré parameter-space shown in the right chart of figure 14, distortions of the imaged diffraction plane lead to small variations, which are the main source of error when performing diffraction measurements with a LEEM instrument and using non-planar foil samples, as has been done in our case. As indicated in the right chart of figure 14, our analysis still allows us to identify the moiré parameters of the analyzed graphene layer on Cu(111) as $\varphi = 22.8° \pm 0.2°$ and $x = 1.038 \pm 0.002$, which is much more precise than simply determining the k-space spot positions of the reciprocal $(1, 0)_{Cu}$ and $(1, 0)_g$ beams. Comparison with first- and second-order commensurability plots for this parameter range verifies that the moiré is most likely incommensurate (see figure SD5 of the supplementary data). Finally, we want to point out that the first-order spots of the identified moiré phase at $\varphi = 22.8° \pm 0.2°$ are not the diffraction spots closest to the (0, 0) beam. As a result, an assignment of the satellite spots of the LEED pattern closest to the (0, 0) beam as first-order moiré beating frequency will lead to a misinterpretation of the data. This fact shows why the outlined analysis addressing all spatial beating frequencies of the moiré phase is mandatory in this case.

4. Conclusions

In the first part of this study we examined the general properties of hexagonal moirés by addressing their symmetry and by analyzing the amount and the k-space position of all spatial beating frequencies present in an nth-order moiré pattern. In particular, by addressing the latter case we could show that any hexagonal moiré can be traced back to spatial beating frequencies that follow circular trajectories in k-space if the two coinciding lattices are rotated one on another. The size and the lateral displacement of the circles have been shown to be affected by the lattice constants of the two coinciding lattices only. Finally, the so-called moiré cell augmentation

method was introduced, which greatly simplifies the search of commensurate moiré phases, as could be explicitly shown by discussing the $(6\sqrt{3} \times 6\sqrt{3})R_{30°}$ moiré of g/SiC(0001). In the second part of this paper, we outlined strategies on how to apply our moiré frequency analysis to experimental SXRD-, STM- and LEED data. Here, we showed that we can extract moiré parameters with high-precision, identifying potential commensurate moiré phases and even treat incommensurate moirés. We also identified certain pitfalls that can be avoided when relating experimental data to *n*th-order commensurability plots. Finally, we pointed out the close relation of multiple scattering during electron diffraction in a LEED experiment and the high-order spatial moiré beating frequencies that can be predicted by our geometrical construction. In this sense, multiple scattering may be regarded as an advantage of the LEED technique, since the knowledge of higher-order spatial moiré frequencies enabled us to determine the graphene lattice strain and alignment with a precision that significantly exceeds the one of an experiment where first-order LEED diffraction spots were analyzed only.

Acknowledgments

We gratefully acknowledge fruitful discussions with Andrea Locatelli, Tefvik Onur Mentes and Alessandro Sala. Furthermore, we thank Matthias Schreck and Michael Weinl for providing the single crystalline Ir(111) films. This work was supported by the German Research Foundation (DFG) in the framework of the Priority Program 1459 'Graphene'.

Appendix A. Experimental details

g/Ir(111)

The graphene growth was performed on thin single crystalline Ir(111) films. The 150 nm thick films were supported by a Si(111) wafer with a buffer layer of yttria stabilized zirconia. A detailed description of the films is given in [50]. The UHV preparation of the Ir films was performed according to [37]. The graphene layer shown in figure 6 was grown by the adsorption of 50 Langmuir ethylene at 2.0×10^{-8} mbar at 300 K followed by annealing to 1073 K. The carbon film was grown and analyzed in a UHV chamber (base pressure in the low 10^{-10} mbar range), which was equipped with a modified SPECS STM 150 Aarhus HT STM. The graphene film shown in figures 7 and 8 were grown by means of CVD at 973 K in an ethylene atmosphere of 2.0×10^{-8} mbar as described in [37]. Growth and analysis was performed in a second UHV chamber with a similar base pressure that hosted a home-built STM.

g/Cu

The graphene growth on copper was carried out on a Cu foil inside a quartz tube reactor. The applied CVD process followed the synthesis strategy described in [51]. The detailed process parameters were: temperature ramping up to 1223 K in $p_{(H2)} = 1$ mbar within 40 min, followed by an oxygen dosing treatment of $p_{(O2)} = 7.5 \times 10^{-6}$ mbar in 1 mbar Ar for 60 min. The subsequent graphene growth was performed at 1348 K at $p = 50$ mbar in a H_2/CH_4 gas mixture of $p_{(H2)}/p_{(CH4)} = 750$ for 2 h (figure 11(a)) and at $p = 15$ mbar in a H_2/CH_4 gas mixture of $p_{(H2)}/p_{(CH4)} = 1000$ for 0.5 h (figures 11(b) and 13). The displayed LEED/LEEM data were acquired using the SPELEEM instrument at the nanospectroscopy beamline of the ELETTRA synchrotron facility [42, 43].

Appendix B

As outlined in section 2.1, we used a coordinate system for the real-space lattice with unit cell definition following the 120° notation. An alternative coordinate system may be chosen, where the real-space is described by unit cell vectors that are rotated by 60° with respect to each other. Since this latter definition is also found in the literature [18], we list in table B1 the conversion of the indexed commensurate moiré unit cells from one notation into the other.

Appendix C. Clockwise and anticlockwise rotation—mirror symmetry

In the following, we prove that a moiré that evolves from a counterclockwise rotation φ of the g-lattice over the TM-lattice has mirror symmetry with respect to the moiré pattern that is generated when performing the same rotation clockwise, i.e. when rotating the g-lattice by $-\varphi$. The mirror symmetry applies with respect to one of the main axes of the non-rotated TM-lattice and occurs for both commensurate and incommensurate moiré

Table B1. Conversion of real-space indexing of commensurate moirés with a moiré unit cell definition following the 120° notation into the one corresponding to the 60° notation and vice versa.

Moiré cell according to the 120° real-space notation		Moiré cell according to the 60° real-space notation
$(m, n)_{\mathrm{TM}}/(r, s)_{\mathrm{g}}$	=>	$(m - n, n)_{\mathrm{TM}}/(r - s, s)_{\mathrm{g}}$
$(m + n, n)_{\mathrm{TM}}/(r + s, s)_{\mathrm{g}}$	<=	$(m, n)_{\mathrm{TM}}/(r, s)_{\mathrm{g}}$

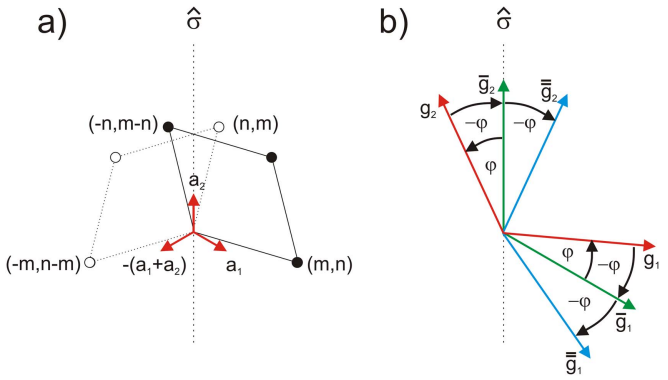

Figure C1. The effect of the mirror operation on a $(m, n)_{\mathrm{TM}}/(r, s)_{\mathrm{g}}$ moiré leading to a moiré pattern that is correctly indexed as $(n, m)_{\mathrm{TM}}/(s, r)_{\mathrm{g}}$. (a) Indexing of the unit cell when relating to the TM-lattice. (b) Applied coordinate transformation when performing the mirror operation on the rotated g-lattice. Please note that the mirror symmetry of the moiré shown in (a) is also reached for the g-lattice after having performed the coordinate transformation into the $\bar{g}$ lattice.

patterns. In the second part or our proof, we show that the mirror symmetry operation on a commensurate $(m, n)_{\mathrm{TM}}/(r, s)_{\mathrm{g}}$ moiré leads to a $(n, m)_{\mathrm{TM}}/(s, r)_{\mathrm{g}}$ moiré, when using the simplified notation of moiré patterns.

Let us first show that the moiré pattern develops mirror symmetry upon a clockwise rotation. For this proof, we mimic the moiré pattern as the product of a lattice function $f_{\mathrm{TM}}(x, y)$ and the rotated lattice function $f_{\mathrm{g}}(x, y)$, i.e. we discuss the function $f_{\mathrm{TM}}(x, y) \times R_{\varphi} f_{\mathrm{g}}(x, y)$, which was introduced in section 1. Using this notation, we will show that:

$$f_{\mathrm{TM}}(x, y) \times R_{-\varphi} f_{\mathrm{g}}(x, y) = \hat{\sigma}\{f_{\mathrm{TM}}(x, y) \times R_{\varphi} f_{\mathrm{g}}(x, y)\}$$

with $\hat{\sigma}$ representing a mirror operation. We choose the real-space lattice functions $f_{\mathrm{TM}}(x, y)$ and $f_{\mathrm{g}}(x, y)$ with the definition of the TM-lattice and its unit vectors $\vec{a}_1$ and $\vec{a}_2$ as already introduced in figure 1. The $\vec{a}_2$ vector of the TM-lattice is aligned along the vertical y-axis and we define $\hat{\sigma}$ without loss of generality as the mirror operation with respect to this axis, i.e. $\hat{\sigma}\{f(x, y)\} = f(-x, y)$. At first we note that:

$$\hat{\sigma}\{f_{\mathrm{TM}} \times f_{\mathrm{g}}\} = \hat{\sigma}\{f_{\mathrm{TM}}\} \times \hat{\sigma}\{f_{\mathrm{g}}\} = \hat{\sigma} f_{\mathrm{TM}} \times \hat{\sigma} f_{\mathrm{g}}.$$

This is obvious, since
$\hat{\sigma}\{f_{\mathrm{TM}}(x, y) \times f_{\mathrm{g}}(x, y)\} = \hat{\sigma}\{f_{\mathrm{TM}}(x, y)\} \times \hat{\sigma}\{f_{\mathrm{g}}(x, y)\} = f_{\mathrm{TM}}(-x, y) \times f_{\mathrm{g}}(-x, y)$. We also have the following identity:

$$R_{-\varphi} = \hat{\sigma}\ R_{\varphi}\ \hat{\sigma}$$

as can be readily verified: $\hat{\sigma} R_{\varphi} \hat{\sigma} = \begin{pmatrix} -1 & 0 \\ 0 & 1 \end{pmatrix} \begin{pmatrix} \cos\varphi & -\sin\varphi \\ \sin\varphi & \cos\varphi \end{pmatrix} \begin{pmatrix} -1 & 0 \\ 0 & 1 \end{pmatrix} = \begin{pmatrix} \cos\varphi & \sin\varphi \\ -\sin\varphi & \cos\varphi \end{pmatrix} = R_{-\varphi}$.

Using these two identities, we can now evaluate:

$$\hat{\sigma}\{f_{\mathrm{TM}} \times R_{\varphi} f_{\mathrm{g}}\} = \hat{\sigma} f_{\mathrm{TM}} \times \hat{\sigma} R_{\varphi} f_{\mathrm{g}} = \hat{\sigma} f_{\mathrm{TM}} \times \hat{\sigma} R_{\varphi} \hat{\sigma} f_{\mathrm{g}} = f_{\mathrm{TM}} \times R_{-\varphi} f_{\mathrm{g}}$$

where we have used the fact that the non-rotated lattices f_{TM} and f_{g} have mirror symmetry with respect to $\hat{\sigma}$ (i.e. $\hat{\sigma} f_{\mathrm{TM}} = f_{\mathrm{TM}}$ and $\hat{\sigma} f_{\mathrm{g}} = f_{\mathrm{g}}$). The above equation shows that the moiré pattern caused by the clockwise rotation of the g-lattice has mirror symmetry with respect to the moiré caused by a counterclockwise rotation. In the case of commensurability, the mirror of the moiré unit cell $(m, n)_{\mathrm{TM}}/(r, s)_{\mathrm{g}}$ is correctly indexed when reversing the order within each tuple, i.e. $(n, m)_{\mathrm{TM}}/(s, r)_{\mathrm{g}}$. This is shown at first for the TM-lattice with the help of figure C1(a). Using the already introduced definition of the TM-lattice with the vectors $\vec{a}_1$ and $\vec{a}_2$ and the chosen mirror operation $\hat{\sigma}$ we can state that:

$$\hat{\sigma}\vec{a}_2 = \vec{a}_2 \text{ and } \hat{\sigma}\vec{a}_1 = -(\vec{a}_1 + \vec{a}_2).$$

The unit cell of the $(m, n)_{TM}/(r, s)_g$ moiré is defined by the vector tuple $[(m, n); R_{120°}(m, n)] = [(m, n); (-n, m - n)]$ when choosing a right-handed coordinate system and relating to the TM-lattice. This unit cell together with the one after the mirror operation is also indicated in figure C1(a).

Using the above definitions, we can calculate the mirror operation on the moiré unit cell as:

$$\begin{aligned}\hat{\sigma}[(m, n); R_{120°}(m, n)] &= \hat{\sigma}[(m, n); (-n, m - n)]\\ &= [(m\hat{\sigma}\vec{a}_1 + n\hat{\sigma}\vec{a}_2); (-n\hat{\sigma}\vec{a}_1 + (m - n)\hat{\sigma}\vec{a}_2)]\\ &= [(-m(\vec{a}_1 + \vec{a}_2) + n\vec{a}_2); (n(\vec{a}_1 + \vec{a}_2) + (m - n)\vec{a}_2)]\\ &= [(-m, n - m); (n, m)] = [R_{120°}(n, m); (n, m)].\end{aligned}$$

The mirror operation transforms the right-handed moiré unit cell into a left-handed one, as can be seen in figure C1(a). If we choose a right-handed notation the sequence of the unit cell vectors has to be reversed, which proves that when relating to the TM-lattice the mirror of a $(m, n)_{TM}$ moiré is correctly indexed as $(n, m)_{TM}$.

The same also holds true for the indexing $(r, s)_g$ when relating to the rotated graphene lattice. This is shown in the following with the help of figure C1(b), which displays the orientation of the unit vectors $\vec{g}_1$ and $\vec{g}_2$ of the g-lattice. Since the g-lattice is rotated by φ with respect to the TM-lattice, it has to be turned backward by -φ so that it reaches the same symmetry properties as the TM-lattice. Therefore, we derive at first a useful expression from the already derived identity: $R_{-\varphi} = \hat{\sigma}\ R_{\varphi}\ \hat{\sigma}$. Multiplying from the right side the operator identity $\hat{\sigma}\ R_{-\varphi}$ leads to:

$$R_{-\varphi}\hat{\sigma}\ R_{-\varphi} = \hat{\sigma}\ R_{\varphi}\ \hat{\sigma}\hat{\sigma}\ R_{-\varphi} = \hat{\sigma}\ R_{\varphi}\ R_{-\varphi} = \hat{\sigma}.$$

As is shown in figure C1(b), we will relate to three differently rotated coordinate systems: the original coordinate system of the moiré $(r, s)_g$ with the g-lattice rotated by φ with respect to the TM-lattice, the one after a subsequent rotation of $-\varphi$, which results in the g-lattice with the $\vec{g}_2$ lattice vector aligned vertically and the coordinates $(r, s)_{\bar{g}}$ and the coordinate system $(r, s)_{\overline{g}}$, which is rotated twice by $-\varphi$. With these abbreviations, we can now calculate the mirror operation to the moiré unit cell vectors when relating to the g-lattice:

$$\begin{aligned}\hat{\sigma}[(r, s)_g; R_{120°}(r, s)_g] &= R_{-\varphi}\hat{\sigma}\ R_{-\varphi}[(r, s)_g; (-s, r - s)_g]\\ &= R_{-\varphi}\hat{\sigma}\ [(r, s)_{\bar{g}}; (-s, r - s)_{\bar{g}}]\\ &= R_{-\varphi}\ [R_{120°}(s, r)_{\bar{g}}; (s, r)_{\bar{g}}]\\ &= [R_{120°}(s, r)_{\overline{g}}; (s, r)_{\overline{g}}].\end{aligned}$$

Here, we could use the fact that after the first rotation $R_{-\varphi}$ the mirror symmetry equivalent to the TM-lattice exists, which leads to the expression in the second row. Again, using the notation of a right-handed system proves that when relating to the g-lattice the mirror of a $(r, s)_g$ moiré is also correctly indexed as $(s, r)_g$. The only difference is that this cell is situated in the g-lattice coordinate system, which is rotated by $-\varphi$ with respect to the TM-lattice.

Appendix D. Analysis of spatial beating frequencies in the second-order moiré g/SiC(0001)

In section 2.6 the usefulness of the cell augmentation concept was discussed using the so-called $(6\sqrt{3} \times 6\sqrt{3})R_{30°}$ moiré found for graphene on SiC(0001) [24]. Apart from the (0, 0) beam and the first-order spots of the SiC-lattice and the g-lattice, ten spatial beating frequencies are identified for the second-order moiré pattern within the sector spanned by the $(1, 0)_{SiC}$ and the $(0, 1)_{SiC}$ reciprocal-space vectors, as displayed in figure 4(d). Following the building principle of second-order moiré beating frequencies, we can list their vector coordinates, which is done in table D1.

As has been shown, the vectors k_1 and k_2 reside on k-space positions that span an incommensurate non-augmented cell, while all other vectors $k_3 \ldots k_{10}$ reside on positions that are members of lattice positions belonging to the commensurate tripled cell of the second-order moiré pattern. One of the six k-space vectors of this commensurate cell is indicated as $K_{moiré}$ in figure 4(d). Table D2 lists possible linear combinations of the identified spatial beating frequencies that equal symmetrically equivalent vectors of $K_{moiré}$.

The respective coordinates relating to the reciprocal-space g-lattice and SiC-lattice can be computed by using table D1. In addition the order of each spatial frequency n_g and n_{SiC} is listed in table D2. The larger of both numbers within each line of the table equals the moiré order n, which would host $K_{moiré}$. Comparing the listed combinations shows that one would identify $K_{moiré}$ in an eighth or higher-order moiré pattern. As a result, the unit cell of the $(6\sqrt{3} \times 6\sqrt{3})R_{30°}$ moiré of g/SiC(0001) can be identified only starting from an eighth-order commensurability plot when relating to a non-augmented moiré cell. This is confirmed by a direct calculation of all spatial beatings frequencies using $\vec{k}_g - \vec{k}_{SiC}$, where $K_{moiré}$ also appears in the eighth-order (not shown). That

Table D1. Coordinates of identified beating frequencies in figure 4(d).

k_1	=	$(1, 1)_g$	—	$(0, 2)_{SiC}$
k_2	=	$(2, \bar{1})_g$	—	$(2, 0)_{SiC}$
k_3	=	$(\bar{1}, 0)_g$	—	$(\bar{1}, \bar{1})_{SiC}$
k_4	=	$(0, 1)_g$	—	$(\bar{1}, 1)_{SiC}$
k_5	=	$(1, \bar{1})_g$	—	$(1, \bar{1})_{SiC}$
k_6	=	$(2, 0)_g$	—	$(1, 1)_{SiC}$
k_7	=	$(\bar{1}, 1)_g$	—	$(\bar{2}, 0)_{SiC}$
k_8	=	$(0, \bar{1})_g$	—	$(0, \bar{2})_{SiC}$
k_9	=	$(0, 2)_g$	—	$(\bar{2}, 2)_{SiC}$
k_{10}	=	$(2, \bar{2})_g$	—	$(2, \bar{2})_{SiC}$

Table D2. Linear combinations of spatial beating frequencies k_i in the second-order moiré cell of the so-called $(6\sqrt{3} \times 6\sqrt{3})R_{30°}$ moiré that lead to the vector $K_{moiré}$ or a symmetrically equivalent one. The resulting coordinates relate to the reciprocal g-lattice and the SiC-lattice. Their respective orders n_g and n_{SiC} are also listed in the table.

Linear combinations leading to $K_{moiré}$ or symmetrically equivalent vectors	n_g	n_{SiC}
$2(k_1 + k_2) - k_3 = (6, 0)_g - (4, 4)_{SiC} - (\bar{1}, 0)_g - (1,1)_{SiC} = (7, 0)_g - (5, 5)_{SiC}$	7	10
$2(k_1 + k_2) - k_4 = (6, 0)_g - (4, 4)_{SiC} - (0, 1)_g - (1, \bar{1})_{SiC} = (6, \bar{1})_g - (5, 3)_{SiC}$	6	8
$2(k_1 + k_2) - k_5 = (6, 0)_g - (4, 4)_{SiC} - (1, \bar{1})_g - (\bar{1}, 1)_{SiC} = (5, 1)_g - (3, 5)_{SiC}$	6	8
$3(k_1 + k_2) - k_6 = (9, 0)_g - (6, 6)_{SiC} - (2, 0)_g - (\bar{1}, \bar{1})_{SiC} = (7, 0)_g - (5, 5)_{SiC}$	7	10
$4(k_1 + k_2) - k_7 = (12, 0)_g - (8, 8)_{SiC} - (\bar{1}, 1)_g - (2, 0)_{SiC} = (13, 1)_g - (10, 8)_{SiC}$	14	18
$4(k_1 + k_2) - k_8 = (12, 0)_g - (8, 8)_{SiC} - (0, \bar{1})_g - (0, 2)_{SiC} = (12, 1)_g - (8, 10)_{SiC}$	13	18
$4(k_1 + k_2) - (1, 0)_g = (12, 0)_g - (8, 8)_{SiC} - (1, 0)_g = (11, 0)_g - (8, 8)_{SiC}$	11	16

the same cell can be identified in a second-order commensurability plot when relating to a tripled cell greatly simplifies the search.

References

[1] Ostyn K M and Carter C B 1982 On the reduction of nickel oxide *Surf. Sci.* **121** 360–74
[2] Chinn M D and Fain S C 1977 Structural phase transition in epitaxial solid krypton monolayers on graphite *Phys. Rev. Lett.* **39** 146–9
[3] Moncton D E, Stephens P W, Birgeneau R J, Horn P M and Brown G S 1981 Synchrotron X-ray study of the commensurate-incommensurate transition of monolayer krypton on graphite *Phys. Rev. Lett.* **46** 1533–6
[4] Wiederholt T, Brune H, Wintterlin J, Behm R J and Ertl G 1995 Formation of two-dimensional sulfide phases on Al(111): an STM study *Surf. Sci.* **324** 91–105
[5] Tetlow H, Posthuma de Boer J, Ford I J, Vvedensky D D, Coraux J and Kantorovich L 2014 Growth of epitaxial graphene: theory and experiment *Phys. Rep.* **542** 195–295
[6] Novoselov K S, Falko V I, Colombo L, Gellert P R, Schwab M G and Kim K 2012 A roadmap for graphene *Nature* **490** 192–200
[7] Wintterlin J and Bocquet M-L 2009 Graphene on metal surfaces *Surf. Sci.* **603** 1841–52
[8] Batzill M 2012 The surface science of graphene: Metal interfaces, CVD synthesis, nanoribbons, chemical modifications, and defects *Surf. Sci. Rep.* **67** 83–115
[9] Hermann K 2012 Periodic overlayers and moiré patterns: theoretical studies of geometric properties *J. Phys. Condens. Matter* **24** 314210
[10] Merino P, Švec M, Pinardi A L, Otero G and Martín-Gago J A 2011 Strain-driven moiré superstructures of epitaxial graphene on transition metal surfaces *ACS Nano.* **5** 5627–34
[11] Zeller P and Günther S 2014 What are the possible moiré patterns of graphene on hexagonally packed surfaces? Universal solution for hexagonal coincidence lattices, derived by a geometric construction *New J. Phys.* **16** 083028
[12] Artaud A, Magaud L, Le Quang T, Guisset V, David P, Chapelier C and Coraux J 2016 Universal classification of twisted, strained and sheared graphene moiré superlattices *Sci. Rep.* **6** 25670
[13] Kawahara K, Arafune R, Kawai M and Takagi N 2015 Pragmatic application of abstract algebra to two-dimensional lattice matching *e-J. Surf. Sci. Nanotechnol.* **13** 361–5
[14] Tkatchenko A 2007 Commensurate monolayers on surfaces: geometry and ground states *Phys. Rev.* B **75** 235411
[15] Pletikosić I, Kralj M, Pervan P, Brako R, Coraux J, N'Diaye A T, Busse C and Michely T 2009 Dirac cones and minigaps for graphene on Ir(111) *Phys. Rev. Lett.* **102** 056808
[16] Wallbank J R, Mucha-Kruczyński M and Fal'ko V I 2013 Moiré minibands in graphene heterostructures with almost commensurate sqrt[3] × sqrt[3] hexagonal crystals *Phys. Rev.* B **88** 155415
[17] Mathieu C, Conrad E H, Wang F, Rault J E, Feyer V, Schneider C M, Renault O and Barrett N 2014 Exploring interlayer Dirac cone coupling in commensurately rotated few-layer graphene on SiC(000-1) *Surf. Interface Anal.* **46** 1268–72
[18] Sato K, Saito R, Cong C, Yu T and Dresselhaus M S 2012 Zone folding effect in Raman *G*-band intensity of twisted bilayer graphene *Phys. Rev.* B **86** 125414
[19] Dedkov Y and Voloshina E 2015 Graphene growth and properties on metal substrates *J. Phys. Condens. Matter* **27** 303002
[20] Xu M, Liang T, Shi M and Chen H 2013 Graphene-like two-dimensional materials *Chem. Rev.* **113** 3766–98

[21] Woods C R *et al* 2014 Commensurate-incommensurate transition in graphene on hexagonal boron nitride *Nat. Phys.* **10** 451–6
[22] Hermann K 2015 *Theory of Moiré Patterns Found for Graphene and Other Overlayers at Metal Surfaces ECSCD-12/European Conference on Surface Crystallography and Dynamics (18–21 October 2015) (Trieste)*
[23] Loginova E, Nie S, Thürmer K, Bartelt N C and McCarty K F 2009 Defects of graphene on Ir(111): rotational domains and ridges *Phys. Rev.* B **80** 085430
[24] Emtsev K V, Speck F, Seyller T, Ley L and Riley J D 2008 Interaction, growth, and ordering of epitaxial graphene on SiC{0001} surfaces: a comparative photoelectron spectroscopy study *Phys. Rev.* B **77** 155303
[25] Martoccia D *et al* 2008 Graphene on Ru(0001): A 25 × 25 supercell *Phys. Rev. Lett.* **101** 126102
[26] Moritz W, Wang B, Bocquet M-L, Brugger T, Greber T, Wintterlin J and Günther S 2010 Structure determination of the coincidence phase of graphene on Ru(0001) *Phys. Rev. Lett.* **104** 136102
[27] Jean F, Zhou T, Blanc N, Felici R, Coraux J and Renaud G 2013 Effect of preparation on the commensurabilities and thermal expansion of graphene on Ir(111) between 10 and 1300 K *Phys. Rev.* B **88** 165406
[28] Blanc N, Jean F, Krasheninnikov A V, Renaud G and Coraux J 2013 Strains induced by point defects in graphene on a metal *Phys. Rev. Lett.* **111** 085501
[29] Zakharchenko K V, Katsnelson M I and Fasolino A 2009 Finite temperature lattice properties of graphene beyond the quasiharmonic approximation *Phys. Rev. Lett.* **102** 046808
[30] Moritz W 2015 LEED studies on modulated surface structures *Z. Kristallogr.* **230** 37–43
[31] Jean F, Zhou T, Blanc N, Felici R, Coraux J and Renaud G 2015 Topography of the graphene/Ir(111) moiré studied by surface x-ray diffraction *Phys. Rev.* B **91** 245424
[32] Singh H P 1968 Determination of thermal expansion of germanium, rhodium and iridium by X-rays *Acta Crystallogr.* A **24** 469–71
[33] Jean F, Zhou T, Blanc N, Felici R, Coraux J and Renaud G 2014 Erratum: effect of preparation on the commensurabilities and thermal expansion of graphene on Ir(111) between 10 and 1300 K [Phys. Rev. B 88, 165406 (2013)] *Phys. Rev.* B **90** 239901
[34] Hattab H *et al* 2012 Interplay of wrinkles, strain, and lattice parameter in graphene on iridium *Nano Lett.* **12** 678–82
[35] Coraux J, N'Diaye A T, Busse C and Michely T 2008 Structural coherency of graphene on Ir(111) *Nano Lett.* **8** 565–70
[36] Donner K and Jakob P 2009 Structural properties and site specific interactions of Pt with the graphene/Ru(0001) moiré overlayer *J. Chem. Phys.* **131** 164701
[37] Zeller P, Dänhardt S, Gsell S, Schreck M and Wintterlin J 2012 Scalable synthesis of graphene on single crystal Ir(111) films *Surf. Sci.* **606** 1475–80
[38] Enachescu M, Schleef D, Ogletree D F and Salmeron M 1999 Integration of point-contact microscopy and atomic-force microscopy: Application to characterization of graphite/Pt(111) *Phys. Rev.* B **60** 16913–9
[39] Ugeda M M, Fernández-Torre D, Brihuega I, Pou P, Martínez-Galera A J, Pérez R and Gómez-Rodríguez J M 2011 Point defects on graphene on metals *Phys. Rev. Lett.* **107** 116803
[40] Davey W P 1925 Precision measurements of the lattice constants of twelve common metals *Phys. Rev.* **25** 753–61
[41] Man K L and Altman M S 2011 Small-angle lattice rotations in graphene on Ru(0001) *Phys. Rev.* B **84** 235415
[42] Locatelli A, Aballe L, Mentes T O, Kiskinova M and Bauer E 2006 Photoemission electron microscopy with chemical sensitivity: SPELEEM methods and applications *Surf. Interface Anal.* **38** 1554–7
[43] Mentes T O, Nino M A and Locatelli A 2011 Spectromicrosocopy with low-energy electrons: LEEM and XPEEM studies at the nanoscale *e-J. Surf. Sci. Nanotech.* **9** 72–9
[44] Rasool H I, Song E B, Allen M J, Wassei J K, Kaner R B, Wang K L, Weiller B H and Gimzewski J K 2011 Continuity of graphene on polycrystalline copper *Nano Lett.* **11** 251–6
[45] Kraus J, Böcklein S, Reichelt R, Günther S, Santos B, Menteş T O and Locatelli A 2013 Towards the perfect graphene membrane?—Improvement and limits during formation of high quality graphene grown on Cu-foils *Carbon* **64** 377–90
[46] Nie S, Wu W, Xing S, Yu Q, Bao J, Pei S-S and McCarty K F 2012 Growth from below: bilayer graphene on copper by chemical vapor deposition *New J. Phys.* **14** 093028
[47] Tang W X, Man K L, Huang H C, Woo C H and Altman M S 2002 Growth shapes of Ag crystallites on the Si(111) surface *Journal of Vacuum Sci. Technol.* B **20** 2492–5
[48] Lim H, Jung J, Yang H J and Kim Y 2014 Lattice-contraction-induced moiré patterns in direction-controlled epitaxial graphene on Cu(111) *Adv. Mat. Interfaces* **1** 1300080
[49] Nakanishi S and Horiguchi T 1981 Surface lattice constants of Si(111), Ni(111) and Cu(111) *Japan. J. Appl. Phys.* **20** L214
[50] Gsell S, Fischer M, Schreck M and Stritzker B 2009 Epitaxial films of metals from the platinum group (Ir, Rh, Pt and Ru) on YSZ-buffered Si(1 1 1) *J. Cryst. Growth* **311** 3731–6
[51] Kraus J, Böbel M and Günther S 2016 Suppressing graphene nucleation during CVD on polycrystalline Cu by controlling the carbon content of the support foils *Carbon* **96** 153–65